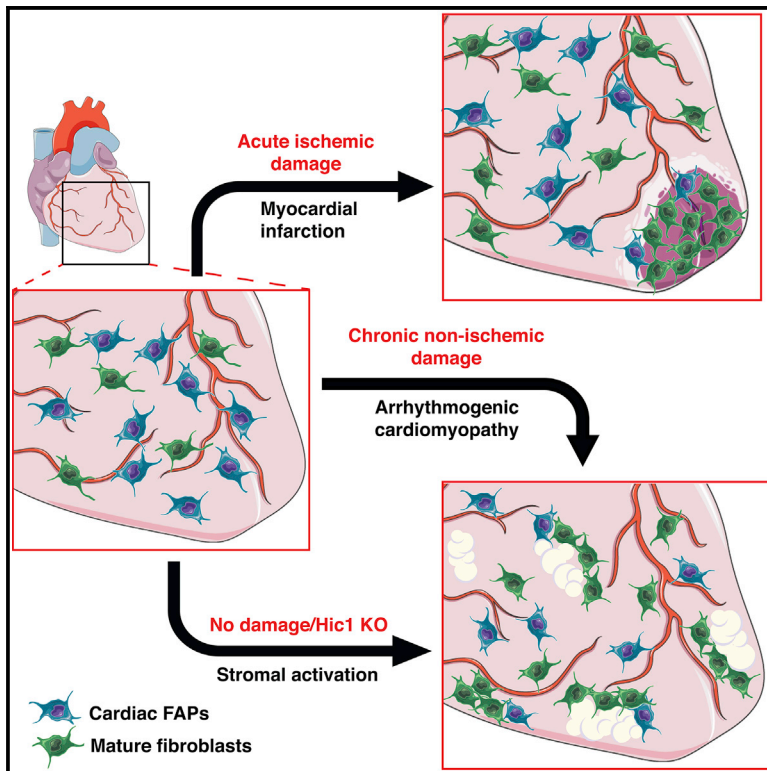


Pathogenic Potential of *Hic1*-Expressing Cardiac Stromal Progenitors

Graphical Abstract



Authors

Hesham Soliman, Ben Paylor,
R. Wilder Scott, ..., Kathleen MacLeod,
T. Michael Underhill, Fabio M.V. Rossi

Correspondence

fabio@brc.ubc.ca

In Brief

Soliman et al. identify a subset of cardiac fibroblasts as multipotent stromal progenitors and describe their dynamic response to damage. Beyond forming the scar, these cells have a pathogenic role in post-myocardial infarction remodeling, and their chronic activation by loss of quiescent factor *Hic1* triggers fibrofatty infiltration and arrhythmogenic cardiomyopathy.

Highlights

- Cardiac PDGFRa⁺ SCA-1⁺ cells (cFAPs) are multipotent mesenchymal progenitors *in vivo*
- PDGFRa⁺ SCA-1⁺ cells differentiate into fibrogenic SCA-1[−] cells upon damage
- Blockade of cFAP differentiation ameliorates cardiac dysfunction post-MI
- Damage-free cFAP activation leads to arrhythmogenic cardiomyopathy



Pathogenic Potential of *Hic1*-Expressing Cardiac Stromal Progenitors

Hesham Soliman,^{1,8} Ben Paylor,¹ R. Wilder Scott,¹ Dario R. Lemos,² ChihKai Chang,¹ Martin Arostegui,¹ Marcela Low,¹ Christina Lee,¹ Daniela Fiore,³ Paola Braghetta,⁴ Vendula Pospichalova,⁵ Christina E. Barkauskas,⁶ Vladimir Korinek,⁵ Alessandra Rampazzo,⁴ Kathleen MacLeod,⁷ T. Michael Underhill,¹ and Fabio M.V. Rossi^{1,9,*}

¹Biomedical Research Centre, University of British Columbia, 2222 Health Sciences Mall, Vancouver, BC V6T 1Z3, Canada

²Harvard Medical School, Boston, MA 02115, USA

³Department of Experimental Medicine, Section of Medical Pathophysiology, Food Science and Endocrinology, Sapienza, University of Rome, Viale Regina Elena 324, 00161 Rome, Italy

⁴Department of Biology, School of Science, University of Padova, Via 8 Febbraio 2, 35122 Padova, Italy

⁵Department of Cell and Developmental Biology, Institute of Molecular Genetics, Academy of Sciences of the Czech Republic, 142 20 Prague 4, Czech Republic

⁶Division of Pulmonary, Allergy, and Critical Care Medicine, Department of Medicine, Duke University, Durham, NC 27710, USA

⁷Molecular and Cellular Pharmacology Research Group, University of British Columbia, 2405 Wesbrook Mall, Vancouver, BC V6T 1Z3, Canada

⁸Faculty of Pharmaceutical Sciences, Minia University, Minia, Egypt

⁹Lead Contact

*Correspondence: fabio@brc.ubc.ca

<https://doi.org/10.1016/j.stem.2019.12.008>

SUMMARY

The cardiac stroma contains multipotent mesenchymal progenitors. However, lineage relationships within cardiac stromal cells are poorly defined. Here, we identified heart-resident PDGFR α ⁺ SCA-1⁺ cells as cardiac fibro/adipogenic progenitors (cFAPs) and show that they respond to ischemic damage by generating fibrogenic cells. Pharmacological blockade of this differentiation step with an anti-fibrotic tyrosine kinase inhibitor decreases post-myocardial infarction (post-MI) remodeling and leads to improvement in cardiac function. In the undamaged heart, activation of cFAPs through lineage-specific deletion of the gene encoding the quiescence-associated factor HIC1 reveals additional pathogenic potential, causing fibrofatty infiltration within the myocardium and driving major pathological features pathognomonic in arrhythmogenic cardiomyopathy (AC). In this regard, cFAPs contribute to multiple pathogenic cell types within cardiac tissue and therapeutic strategies aimed at modifying their activity are expected to have tremendous benefit for the treatment of diverse cardiac diseases.

INTRODUCTION

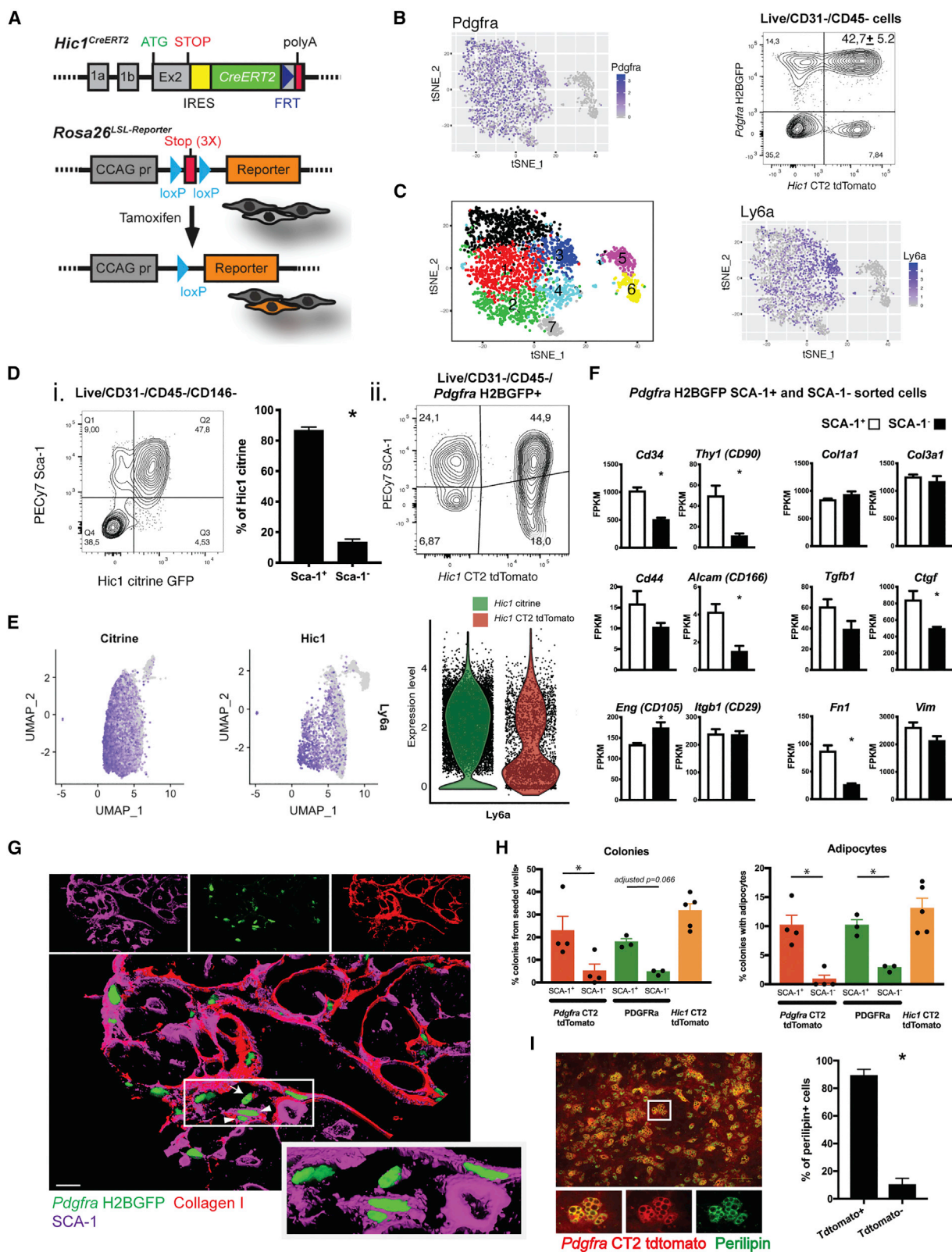
The cardiac stroma has important roles in both homeostasis and remodeling after damage. In the aftermath of myocardial infarction (post-MI), stromal cells activate a fibrogenic program that eventually leads to the replacement of lost cardiac muscle with a fibrous scar (Frangogiannis, 2012). In that case, fibrogenic cells

take on a reparative role because scar formation is critical to maintaining appropriate cardiac function and integrity (Frantz et al., 2008; Ikeuchi et al., 2004). However, chronic interstitial fibrosis is also a common outcome of myocardial infarction, and the persistent activation of a fibrogenic program can contribute to cardiac pathology and disease progression (See et al., 2005). However, the cellular and molecular mechanisms leading to accumulation of fibrogenic cells within the heart are poorly understood, limiting our ability to modulate them therapeutically.

Tissue-resident cardiac stromal cells have been shown to give rise to multiple lineages, including fibrogenic cells, committed osteoprogenitors, and adipocytes (Chong et al., 2011). These findings suggested that a mesenchymal hierarchy exists within the adult heart, comprising immature progenitors that give rise to more differentiated cell types. Cardiac fibroblasts, defined based on the expression of classical markers, such as *Col1a1*, *Tcf21*, and *Pdgfra*, are heterogeneous and encompass several phenotypically and functionally distinct cellular subsets (Pinto et al., 2016). This lack of uniformity suggests that mesenchymal progenitors, defined as the cells that maintain and repair connective tissue, may have been included in such a definition. Indeed, significant phenotypic similarities between classical cardiac fibroblasts and mesenchymal progenitors have been reported (Haniffa et al., 2009; Hematti, 2012).

We and others have identified a population of tissue-resident multipotent stromal cells in skeletal muscle that is characterized by the expression of PDGFR α and the stem cell marker SCA-1 (Joe et al., 2010; Uezumi et al., 2010). Those cells are referred to as fibro-adipogenic progenitors (FAPs) because of their propensity to generate fibroblasts as well as adipocytes. In addition, they can be induced to acquire an osteogenic fate upon treatment with BMP2, further supporting the notion that FAPs are multipotent progenitors (Pillai et al., 2017). Phenotypically identical cells with similar lineage potential were also found in numerous other tissues, including bone, kidney, skin (Festa





(legend on next page)

et al., 2011), fat (Chun et al., 2013), and heart (Chong et al., 2011). These populations have been shown to possess highly similar transcriptomes, albeit with some tissue-specific differences in gene expression patterns (Pelekanos et al., 2012).

Interestingly, unlike in skeletal muscle in which all PDGFRa⁺ cells express SCA-1, in the adult heart, at steady state, a subpopulation of PDGFRa⁺ cells are SCA-1[−]. Here, we show that a large fraction of stromal cells thought to be mature cardiac fibroblasts are, in fact, multipotent progenitors, as defined by their *in vitro* clonogenicity and *in vivo* and *in vitro* lineage potential. These progenitors generate PDGFRa⁺ and SCA-1[−] fibroblasts upon injury, and pharmacological inhibition of this differentiation step improves cardiac function post-MI. Impairing the ability of these cells to remain quiescent by deletion of the transcription factor HIC1 leads to fibrofatty infiltration and arrhythmias in the absence of primary cardiomyocyte damage. Consistent with that, lowering the cardiac FAPs (cFAPs) threshold of activation in arrhythmogenic cardiomyopathy (AC) leads to earlier onset and increased severity of the pathology.

RESULTS

Hic1 Expression Identifies a Population of Cardiac Stromal Cells Enriched in Multipotent Mesenchymal Progenitors

HIC1 was recently proposed as a transcription factor expressed in stromal progenitors (Scott et al., 2019). To analyze the population of Hic1-expressing stromal cells within the heart and gain a better understanding of their lineage capabilities *in vivo*, we took advantage of a double-transgenic mouse carrying both tamoxifen (TAM)-inducible Cre recombinase inserted in the Hic1 locus and the floxed tdTomato (Rosa^{LSL-tdTomato}) reporter (Hic1-CreERT2 or Hic1-CT2 tdTomato; Figure 1A). TAM treatment in these mice leads to indelible labeling of Hic1-expressing cells and their progeny with tdTomato, allowing lineage tracing. Ten days after TAM treatment, cardiac tdTomato⁺ cells were sorted and analyzed by single-cell (sc) RNA sequencing (RNA-seq) to evaluate population heterogeneity. Principal component analysis, followed by dimensionality reduction, revealed two spatially distinct clusters of cells; of which the largest represented Pdgfra⁺ stromal cells (Figures 1B, left, and S1A), and the other an as yet uncharacterized Pdgfra[−], Ly6a[−] (the

gene encoding SCA-1) cell type expressing mural cell markers, which is the subject of an ongoing study (Figure S1B). We confirmed the overlap between Hic1 and Pdgfra expression by performing flow cytometry on the hearts of Hic1 CT2 tdTomato mice that also expressed H2B-EGFP from the Pdgfra locus (Figure 1B, right). Additionally, immunostaining revealed that Hic1 tdTomato co-localized with Pdgfra H2BGFP or the mural cell marker NG2 (Figure S1C).

Expression of PDGFRa is commonly used to identify stromal cells (Farbehi et al., 2019; Joe et al., 2010; Skelly et al., 2018; Uezumi et al., 2010). However, this population is highly heterogeneous (Farbehi et al., 2019). Indeed, cluster analysis of the Pdgfra⁺ cells revealed six different subclusters (Figure 1C, left). Interestingly, cells expressing the highest levels of the progenitor cell marker Ly6a/SCA-1 (Figure 1C, right) were assigned to the same subcluster (subcluster 3 in Figure 1C and indicated by an arrowhead in Figure S1D), suggesting that this marker may identify a cell type expressing a distinctive transcriptional program within the Hic1 CT2 tdTomato⁺ Pdgfra⁺ cells. Figure S1E shows a heatmap of the top-10 most differentially expressed genes in each of the Pdgfra⁺ subclusters.

To further investigate the relationship between SCA-1 and Hic1 expression, we compared cells from the hearts of Hic1 CT2 tdTomato mice with those of mice carrying citrine GFP knocked into the Hic1 locus (Hic1-citrine), which labels only cells expressing Hic1 and not their progeny (Pospichalova et al., 2011). We found that, although Hic1 expression after excluding mural cells was enriched in cells expressing SCA-1 (although a population of SCA-1[−] cells was also labeled; Figure 1D, i), their tdTomato⁺ progeny included a larger fraction of SCA-1[−] cells (Figure 1D, ii). This was confirmed by scRNA-seq of Hic1-citrine⁺ cells in the heart, which revealed that the frequency of Ly6a/SCA-1[−] cells in this population was lower than observed in the Hic1 CT2 tdTomato-labeled cells (Figure 1E). Based on our previous studies in skeletal muscle (Joe et al., 2010; Uezumi et al., 2010), we hypothesized that Hic1⁺ Pdgfra⁺ SCA-1⁺ cells may be endowed with progenitor properties and the more differentiated Hic1[−] Pdgfra⁺ SCA-1[−] cells may represent their progeny.

To further assess differences between Pdgfra⁺ SCA-1⁺ and SCA-1[−] cells, we sorted each subset from the stromal fraction (CD45[−]/CD31[−]/Pdgfra H2BGFP⁺). Initial analysis showed that, compared to CD45[−]/CD31[−]/Pdgfra[−] cells, both Pdgfra⁺

Figure 1. The PDGFRa⁺ SCA-1⁺ Subset of Cardiac Fibroblasts Contains Multipotent Mesenchymal Progenitors

- (A) Schematic of the Hic1 CT2 and Rosa26^{LSL-Reporter} alleles.
 (B) Feature plot of Hic1 CT2 tdTomato⁺ cells in the heart, showing Pdgfra expression (left). Representative FACS plot of Pdgfra H2BGFP⁺ and Hic1 CT2 tdTomato⁺ cells in the heart (right).
 (C) T-distributed stochastic neighbor embedding (t-SNE) clustering plots of Hic1 CT2 tdTomato⁺ cells in the heart (left) and expression of Ly6a/SCA-1 (right).
 (D) (i) Representative FACS plot and quantification of the CD45[−] CD31[−] CD146[−] SCA-1⁺ and SCA-1[−] cells in the heart that are Hic1 citrine⁺. (ii) Representative FACS plot of CD45[−] CD31[−] Pdgfra H2BGFP⁺ SCA-1⁺ and SCA-1[−] that were Hic1 CT2 tdTomato⁺ (n = 3).
 (E) Feature and violin plots of Ly6a/SCA-1 expression after integration of the single-cell RNA expression profiles of Hic1 CT2 tdTomato- and Hic1 citrine-labeled cells in undamaged hearts.
 (F) Quantification of RNA expression levels of the mentioned genes in Pdgfra H2BGFP⁺ SCA-1⁺ and SCA-1[−] cells in undamaged heart (n = 4 for SCA-1[−]; n = 5 for SCA-1⁺ groups).
 (G) Representative 3D reconstruction of a z stack of images of collagen I and SCA-1 immunostaining of 10-μm cryosections from the left ventricular free wall of undamaged Pdgfra H2BGFP mice hearts. Inset: zoomed image of the area highlighted by the white rectangle. Arrowheads indicate SCA-1⁺ cells, and arrows indicate SCA-1[−] cells. Scale bar: 20 μm.
 (H) Clonal expansion and adipogenic potential of Pdgfra CT2 tdTomato⁺ or PDGFRa⁺/SCA-1⁺ and SCA-1[−], and MCAM[−]/Hic1 CT2 tdTomato⁺ cells, (n = 3–5 mice).
 (I) Representative image and quantification of perilipin⁺/Pdgfra CT2 tdTomato⁺ adipocytes (n = 4 in each group). Scale bar: 100 μm.
 Data in the graphs in Figure 1 are represented as means ± SEM. *p < 0.05 compared with other groups or as indicated by a horizontal bar.

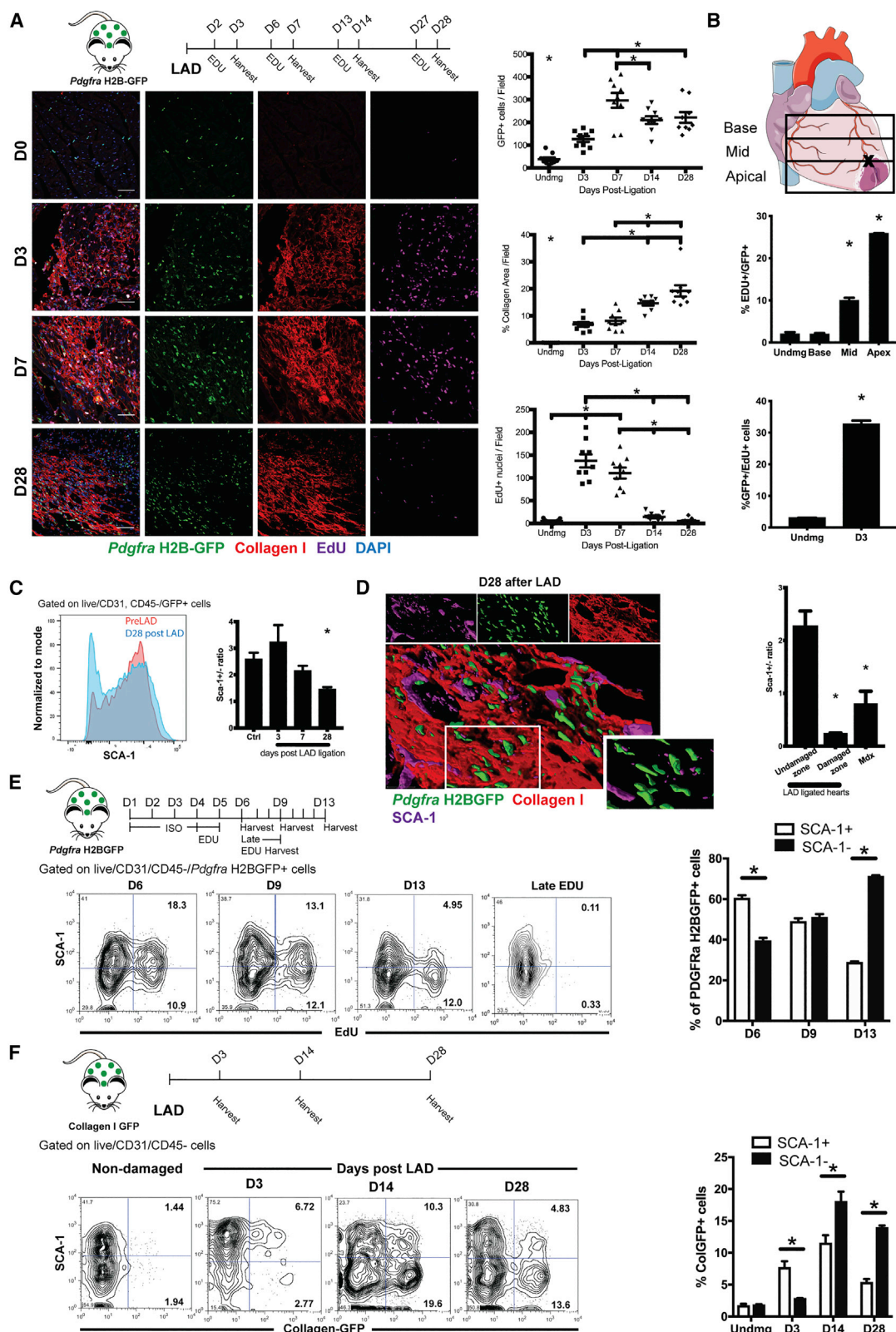


Figure 2. Response of Cardiac PDGFR α ⁺ Cells to Myocardial Damage

(A) Schematic of the LAD ligation injury experiment in *Pdgfra* H2BGFP mice (top left). Representative images (bottom left) and quantification (right) of GFP⁺ cells, collagen I, and EdU in 10- μ m cryosections from undamaged or LAD-ligated hearts ($n = 9$ /group; scale bar: 60 μ m).

(legend continued on next page)

populations were enriched for extracellular matrix (ECM)-associated genes (Figure S1F), confirming their stromal nature (Ieronimakis et al., 2013). Bulk RNA-seq showed that the SCA-1⁺ population expressed significantly more mesenchymal progenitors-associated markers compared with that of SCA-1[−] cells, including *Thy1*(Cd90), *Cd44*, and *Cd34* (Figure 1F), as well as a set of markers (*Dpp4*, *Wnt2*, *Pi16*, and *Anxa3*), recently identified as markers of adipose tissue multipotent interstitial progenitors (Merrick et al., 2019) (Figure S1G). In contrast to previous reports (Ieronimakis et al., 2013), however, we failed to detect distinct anatomical locations for cardiac PDGFRa⁺/SCA-1⁺ and PDGFRa⁺/SCA-1[−] cells, which we found to be in close proximity (Figures 1G and S1H). Thus, in the resting heart, both SCA-1⁺ and SCA-1[−] cell types express similar transcriptional programs indicative of a fibrogenic potential, and their transcriptome or anatomical locations fails to distinguish them functionally.

We confirmed that *Pdgfra*-H2BGFP faithfully recapitulates endogenous PDGFRa expression using both immunostaining of sections (Figure S1I) and flow cytometry (Figure S1J). This was still evident after induction of myocardial infarction by left anterior descending coronary artery (LAD) ligation, despite a reduction in *Pdgfra* expression (Figure S1J). scRNA-seq on purified *Pdgfra* H2BGFP⁺ cells confirmed, consistent with a recent report (Farbehi et al., 2019), that *Pdgfra* expression is restricted to cFAPs and fibroblasts and is not present in other cardiac cells, even after damage (Figure S1K). To further analyze the stromal population, we took advantage of a recently published mouse strain (Chung et al., 2018) expressing a TAM-inducible CRE recombinase inserted into *Pdgfra* locus. Because this strain was not characterized in the heart, we labeled cells from *Pdgfra* CT2 tdTomato⁺ animals with anti-PDGFRa antibody and found complete overlap both by immunostaining (Figure S2A) and by flow cytometry (Figure S2B). After LAD ligation, PDGFRa expression was downregulated, whereas *Pdgfra* CT2 tdTomato labeling, typical of lineage tracing strategies, was not (Figure S2B). In addition, we assessed spontaneous recombination before and after myocardial infarction and detected very few tdTomato⁺ cardiomyocytes and rare stromal cells, validating the use of this strain (Figures S2C–S2E). Additionally, we did not detect spontaneous recombination in the *Hic1* CT2 tdTomato mice in undamaged hearts or after LAD ligation (Figure S2C).

To assess the *in vitro* potential of these cells, we purified them as either from *Pdgfra* CT2 tdTomato hearts, based on tdTomato

expression, or from ubiquitous GFP animals, based on staining with PDGFRa antibody and SCA-1⁺ or SCA-1[−] cells were individually seeded. Although all colonies contained α SMA⁺ myofibroblasts (data not shown), the clonogenicity and differentiation potential toward adipocytes (Figure 1H) of SCA-1⁺ cells was markedly greater than it was for SCA-1[−] cells, consistent with the premise that the latter may represent a more-differentiated progeny. Next, we compared *Hic1* CT2 tdTomato⁺ cells (soon after TAM) to *Pdgfra* CT2 tdTomato⁺ SCA-1⁺ cells. *Hic1*-labeled cells were divided into MCAM⁺ (mural cells) and MCAM[−] cells, and we found that only the MCAM[−] fraction (containing cFAPs) formed colonies (data not shown for MCAM⁺ cells). The lineage potential and clonogenicity of *Hic1* CT2 tdTomato⁺ cells was comparable to *Pdgfra* CT2 tdTomato/SCA-1-labeled cells, supporting the notion that they represent similar populations (Figure 1H). To assess whether other cells contribute to adipogenic activity in the heart, bulk cultures from *Pdgfra* CT2 tdTomato mice were expanded in adipogenic media. As shown in Figure 1I, most perilipin⁺ adipocytes were tdTomato⁺, suggesting that *Pdgfra*⁺ cells are the main contributors to adipocyte formation in the heart. Thus, a significant proportion of PDGFRa⁺/SCA-1⁺ cells, which had been previously defined as cardiac fibroblasts (Pinto et al., 2016), behave as multipotent mesenchymal progenitors *in vitro*, similar to skeletal muscle-derived FAPs (Joe et al., 2010; Uezumi et al., 2010).

Stromal Dynamics in the Acutely Damaged Myocardium

Induction of experimental infarction in *Pdgfra* H2BGFP mice (Hamilton et al., 2003) resulted in a significant increase in *Pdgfra* H2BGFP⁺ cells (Figure 2A), correlating with proliferation in the damaged apical region of the heart, in which more than 30% of EdU⁺ cells were GFP⁺ (Figures 2A and 2B). In contrast to skeletal muscle injury, in which FAPs numbers rapidly return to pre-injury levels, the increase in cFAPs after damage was sustained over time (Figure 2A). Additionally, in contrast to undamaged areas in which most of the *Pdgfra* H2BGFP⁺ cells remained positive for SCA-1, we observed a time-dependent decrease in the ratio of SCA-1⁺ to SCA-1[−] cells in the damaged heart apex (Figure 2C). Interestingly, this decrease in SCA-1⁺/SCA-1[−] ratio was concomitant with a reduction in *Pdgfra* H2BGFP expression (Figure S3A), suggesting that injury induces a differentiation trajectory characterized by downregulation of both markers.

(B) Diagram to show where hearts, after LAD ligation, were cut and divided into apical, mid, and basal sections (top). Quantification of the percentage of *Pdgfra* H2BGFP⁺ that was also EdU⁺ in the apical, mid, and basal sections of the heart 3 days after LAD ligation (mid; n = 2/group). Quantification of the percentage of EdU⁺ cells that was also *Pdgfra* H2BGFP⁺ in the apical region of the heart 3 days after LAD ligation (bottom; n = 3/group).

(C) Representative FACS histogram showing SCA-1 staining in undamaged (pre-LAD) and 28 days after LAD-ligated (D28 after LAD) hearts (left) and quantification of the SCA-1⁺/SCA-1[−] ratio in the *Pdgfra* H2BGFP⁺ cells (right). Only the apical region was used (n = 3 in all groups, except 28 days after LAD for which n = 4).

(D) Representative 3D reconstruction of a z stack of images of collagen I and SCA-1 immunostaining of 10- μ m cryosections from *Pdgfra* H2BGFP mice hearts 28 days after LAD ligation (left). Inset: zoomed image of the area highlighted by the white rectangle showing *Pdgfra* H2BGFP and SCA-1 staining only. Scale bar: 20 μ m. Quantification of the SCA-1⁺/SCA-1[−] ratio in *Pdgfra* H2BGFP⁺ population in sections from 28 days after LAD ligation or 1-year-old mdx mice hearts (right; n = 3 for LAD-damaged and mdx hearts; n = 4 for undamaged hearts).

(E) Schematic of the experimental design (top left). Representative FACS plots (bottom left) and quantification (right) of the percentage of EdU⁺ *Pdgfra* H2BGFP⁺ SCA-1⁺ or SCA-1[−] (relative to the total of EdU⁺ cells) at different time points after ISO treatment. D6, D9, and D13 are the first, fourth, and eighth days, respectively, after ISO treatment.

(F) Schematic of the experimental design (top left). Representative FACS plots (bottom left) and quantification (right) of the percentage of *Col1a1*-3.6GFP⁺ cells that were SCA-1⁺ or SCA-1[−] in undamaged hearts and at days 3, 14, and 28 after LAD ligation (n = 4).

Data in the graphs in Figure 2 are represented as means \pm SEM. *p < 0.05 compared with other groups or as indicated by a horizontal bar.

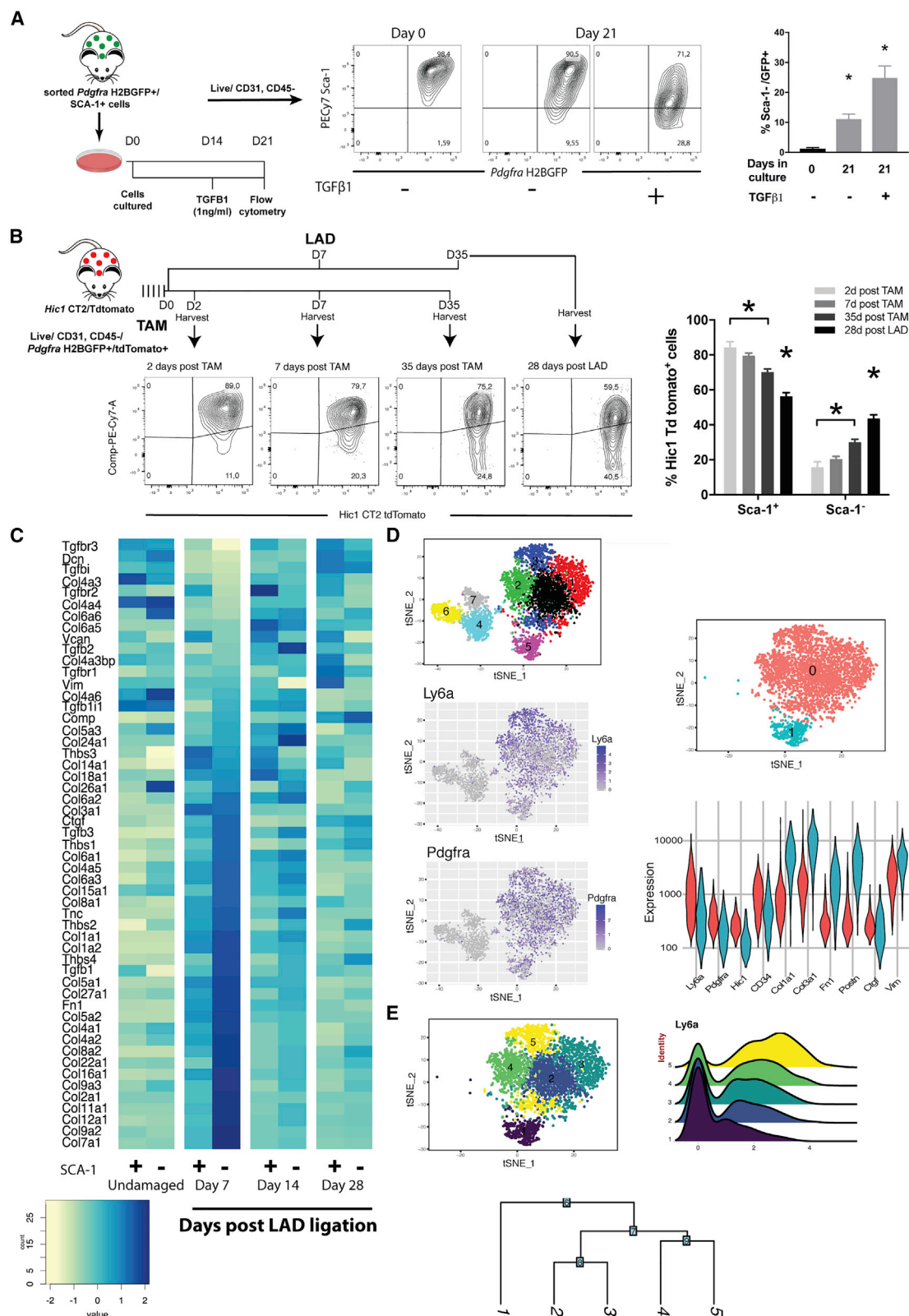


Figure 3. SCA-1⁺ Cells Represent Progenitors for the More-Fibrogenic SCA-1⁻ Cells

(A) Schematic of the experimental design (left). Representative FACS plots (middle) and quantification (right) of the percentage of *Pdgfra* H2BGFP⁺ cells that became SCA-1⁺ by day 21 in culture in the absence or presence of TGF-β (1 ng/mL) treatment for the previous 7 days (n = 3).

(legend continued on next page)

Because LAD ligation does not produce transmural infarctions in our hands, we focused our analysis on the damaged areas only, identified by the presence of collagen I deposits. In those locations, more than 80% of the GFP⁺ cells failed to stain for SCA-1 (Figures 2D and S3B). Thus, SCA-1[−] cells increase upon damage, and they preferentially localize to areas of collagen deposition.

To assess the proliferation kinetics of PDGFRα⁺ cells, we switched to a model of damage amenable to greater throughput analysis. We injected *Pdgfra* H2BGFP mice with isoproterenol (ISO) for 5 consecutive days (100 mg/kg, subcutaneously [s.c.]), a treatment known to induce subendocardial ischemic damage (Heather et al., 2009). EdU was administered once daily (1 mg/day) in the final 2 days of ISO treatment. Twenty-four hours later, more than 50% of the EdU⁺ cells were GFP⁺ (Figure S3C). Although, at that time point, EdU incorporation was predominantly detected in SCA-1⁺ cells, 7 days later most labeled cells were SCA-1[−] (Figure 2E). Importantly, no incorporation was observed when EdU was injected 3 days after the end of ISO treatment (Figure 2E), indicating that any EdU positivity observed past that time must be due to inheritance of the label from ancestral cells that were proliferating at the time of EdU administration. This strongly suggests that SCA-1⁺ cells initially respond to damage by proliferating, and eventually by generating SCA-1[−] progeny. The fact that SCA-1[−] cells retain the label for more than a week past the end of EdU administration additionally indicates that their proliferative capacity is limited, in accordance with our *in vitro* data.

The association of SCA-1[−] cells with collagen-rich regions prompted us to investigate collagen expression in *Pdgfra*⁺ cells. To that end, we induced LAD ligation in mice carrying EGFP under the control of a *Col1a1* regulatory region (Kalajzic et al., 2002). Similar to what was observed with EdU, early after damage, EGFP expression was mainly associated with the SCA-1⁺ fraction, whereas, at later stages, it gradually shifted to SCA-1[−] cells (Figure 2F). This is again consistent with SCA-1[−] cells being the differentiated fibrogenic progeny of SCA-1⁺ progenitors.

Transforming growth factor (TGF)-β is known to induce a fibrogenic program in mesenchymal progenitors. To test whether that was associated with downregulation of SCA-1, we sorted *Pdgfra* H2BGFP⁺/SCA-1⁺ cells and cultured them. A small population of SCA-1[−] cells was generated during the first week of culture in the absence of TGF-β1, but did not increase in the following 2 weeks (data not shown). As SCA-1[−] cells do not expand as efficiently in culture, this suggests that their numbers reached an equilibrium because of their continued production and dilution by prolifer-

ating SCA-1⁺ progenitors. Treatment with TGF-β1 for 7 days led to a doubling of SCA-1[−] cells in culture, consistent with the notion that SCA-1 downregulation parallels the adoption of a fibrogenic fate (Figure 3A). In aggregate, this body of *in vitro* results supports the hypothesis that SCA-1⁺ cells represent progenitors for fibrogenic SCA-1[−] cells.

We further tested the relationship between SCA-1⁺ and SCA-1[−] cells by lineage tracing in the *Hic1*-CT2 mouse strain. As expected, when animals were harvested immediately after the end of TAM treatment, tdTomato⁺ cells were enriched in SCA-1⁺ cells (D2 in Figure 3B). Modest increases in the frequency of SCA-1[−] cells were detected 7 and 35 days after TAM (D7 and D35 in Figure 3B), suggesting that, similar to what was observed *in vitro*, low-level homeostatic production of these cells takes place in the absence of overt damage. LAD ligation significantly increased the generation of SCA-1[−] cells, which reached approximately 50% of the labeled population 4 weeks after the surgery (Figure 3B). A caveat of this experiment is that a population of SCA-1[−] cells was also labeled by *Hic1*-CT2 tdTomato immediately after TAM treatment (D2 in Figure 3B), and, therefore, the observed results may also be explained by their preferential expansion. To further investigate that possibility, we delivered 6-h pulses of EdU to undamaged mice and found that the SCA-1⁺ showed significantly greater percentage EdU positivity (1.89% ± 0.2%) than did the SCA-1[−] population (0.96% ± 0.1%), ruling out the possibility that preferential proliferation caused the shift in their ratios. Thus, both in homeostasis and at an increased rate after damage, SCA-1⁺ cFAPs generate SCA-1[−] cells.

To examine in more depth the phenotype of the SCA-1⁺ and SCA-1[−] populations, we performed RNA-seq on fluorescence-activated cell sorting (FACS)-sorted *Pdgfra* H2BGFP⁺ cells before damage and at 1, 2, or 4 weeks after LAD ligation. No overt differences in ECM-related gene expression was detected between SCA-1⁺ and SCA-1[−] cells at homeostasis or 4 weeks after surgery (Figure 3C). However, transcripts associated with pathologic matrix deposition were markedly enriched in the SCA-1[−] fraction 1 and 2 weeks after damage (Figure 3C). In accordance with that, clustering of scRNA-seq data from *Hic1*-CT2 tdTomato⁺ cells 7 days after LAD ligation revealed two spatially distinct clusters expressing *Pdgfra*; one of which expressed lower levels of *Ly6a*/SCA-1 and *Hic1* but was highly enriched for ECM-related genes as well as the activated fibroblast marker *periostin* (Kanisicak et al., 2016) (Figure 3D).

Clustering analysis revealed that the *Pdgfra*⁺ cells retained their heterogeneity after damage (Figure 3D) and that the cells expressing highest levels of *Ly6a*/SCA-1 still grouped together

(B) Schematic of the experimental design (top left). Representative FACS plots (bottom left) and quantification (right) of the percentage of *Pdgfra* H2BGFP⁺/*Hic1* CT2 tdTomato⁺ cells that were either SCA-1⁺ or SCA-1[−] at different time points after TAM injection in undamaged or LAD-ligated mice hearts (n = 3 for the 7 days after TAM group; n = 4 in all other groups).

(C) Heatmap of the relative expression of key fibrogenic genes produced from sorted and RNA-sequenced *Pdgfra* H2BGFP⁺ SCA-1⁺ or SCA-1[−] cells in undamaged or LAD-ligated hearts at different time points after injury. The heatmap was generated from the z score of the different genes at the specified time points (n = 4–5 for undamaged, n = 3 for 7 days, n = 2 for 14 days, and n = 3–4 for 28 days after LAD).

(D) t-SNE and violin plots of single-cell RNA-sequenced *Hic1* CT2 tdTomato⁺ cells isolated from the apical (damaged) region of the heart 7 days after LAD ligation. Illustration of the expression of *Pdgfra* and *Ly6a*/SCA-1 (top), whereas the other panel shows a violin plot of the expression of genes of interest in the two clusters expressing *Pdgfra* (bottom).

(E) *Pdgfra*⁺ cells were subset from the *Hic1* CT2 tdTomato⁺ population (top left). Ridge plot of *Ly6a*/SCA-1 expression in the different clusters (top right). Phylogenetic tree of the *Pdgfra*⁺ clusters based on cluster similarity (bottom).

Data in the graphs in Figure 3 are represented as means ± SEM. *p < 0.05 compared with all other groups or as indicated by a horizontal bar.

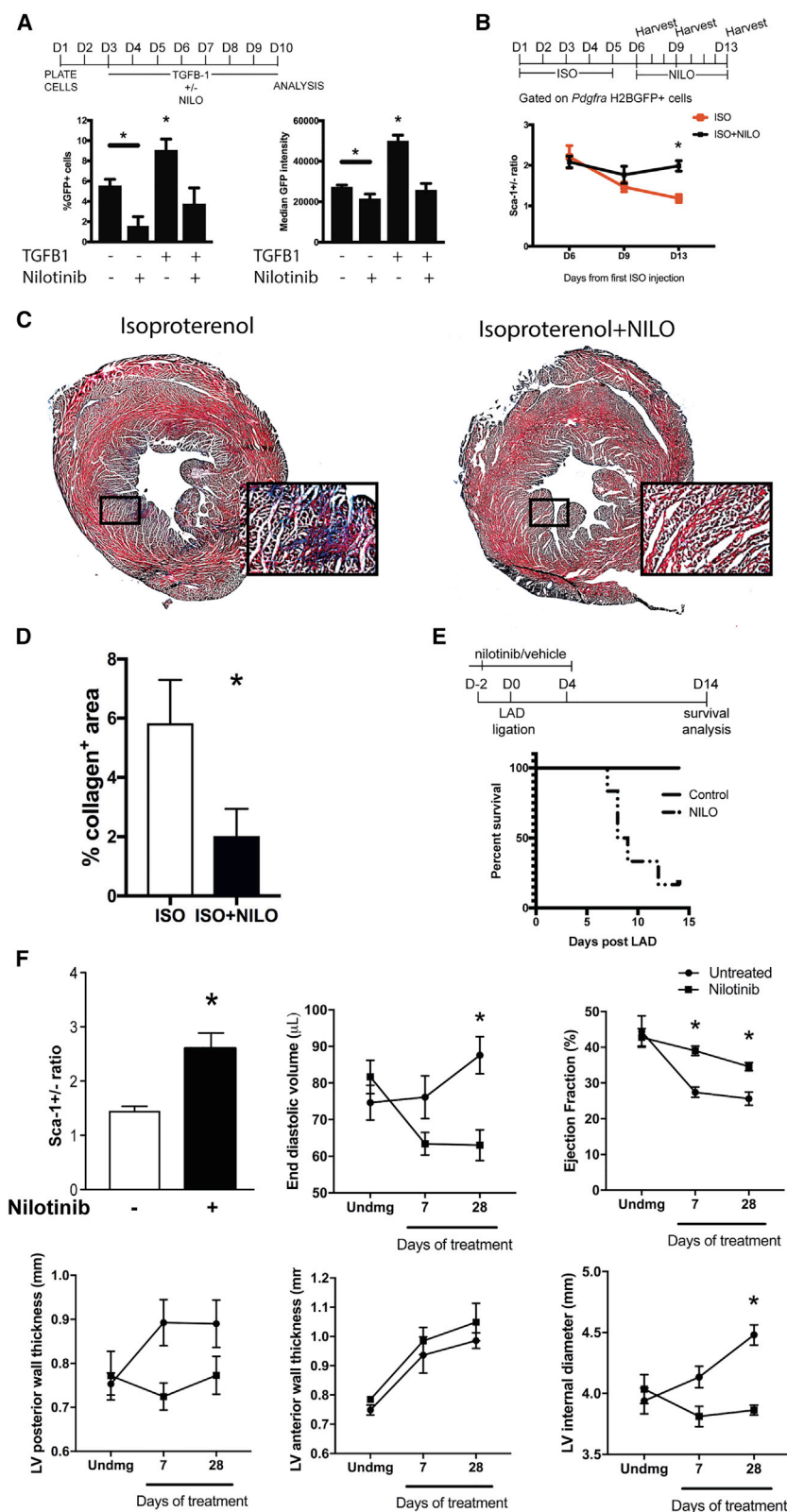


Figure 4. Inhibition of cFAP Differentiation Improves Cardiac Performance

(A) Schematic of the experimental design and quantification of the percentage of *Col1a1*-3.6GFP⁺ cells and median GFP intensity in sorted SCA-1⁺ cells cultured for 7 days ± TGF-β (1 ng/mL) or nilotinib (1 μM; n = 6 wells for control and TGF-β groups, n = 7 for nilotinib-only group, and n = 9 in TGF-β + nilotinib). (B) Schematic of experimental design and quantification of the SCA-1⁺/SCA-1⁻ cell ratio in *Pdgfra* H2BGFP⁺ population in the heart at different time points after ISO treatment (n = 3 in all groups, except D13 groups, in which n = 4).

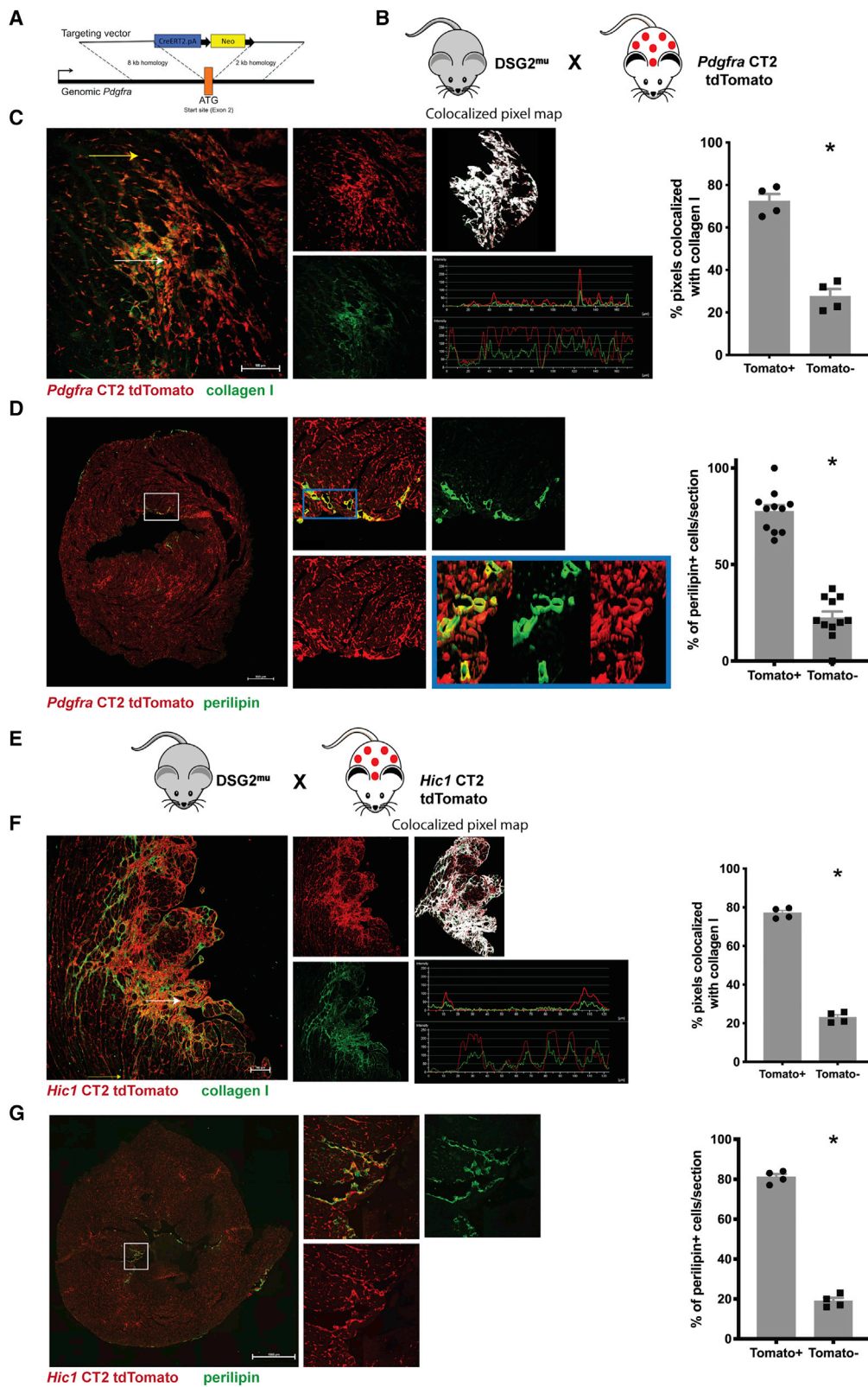
(C) Photomicrographs of heart sections from ISO-treated mice ± nilotinib, stained with Masson's trichrome staining. The insets are zoomed views of the areas outlined by the black rectangles.

(D) Quantification of collagen-I-immunostained area in heart sections of *Pdgfra* H2BGFP mice treated with ISO (100 mg/kg) ± nilotinib (25 mg/kg; n = 5).

(E) Schematic of the experimental design and Kaplan-Meier survival curve of mice treated with nilotinib or vehicle for 7 days starting 2 days before LAD ligation (n = 5–6).

(F) Effect of nilotinib on the SCA-1⁺/SCA-1⁻ ratio in *Pdgfra* H2BGFP⁺ cells and on cardiac function after LAD ligation. n = 5 for undamaged, n = 6 for 7-days untreated, n = 7 for 7 and 28 days of nilotinib treatment, and n = 11 for 28-day untreated group.

Data in the graphs in Figure 4 are represented as means ± SEM. *p < 0.05 compared with other groups or as indicated by a horizontal bar. In the line graphs, *p < 0.05 compared with other group at the same time point.



(legend on next page)

(subcluster 3 in Figures 3D and S4A). Figure S4B shows a heatmap of the top 10 most differentially expressed genes in each of the *Pdgfra*⁺ subclusters.

Interestingly, when the *Pdgfra*⁺ clusters were organized in a phylogenetic tree, the resulting hierarchy correlated with the level of *Ly6a* expression (Figure 3E). This further supports the hypothesis that cells downregulate SCA-1 as they differentiate along the fibrogenic lineage and that multiple intermediate states may be generated within the SCA-1⁺ to SCA-1[−] continuum.

To further explore relationships among *Pdgfra*⁺ cells, we performed single-cell trajectory inference with the Monocle R package, which separated cells into seven clusters (Figure S4C, i and ii). Cells were ordered along a branched trajectory (Figure S4C, ii), and pseudotime analysis showed that clusters with greatest *Ly6a* expression bifurcated into two branches (Figure S4C, iii and iv); one of which is dominated by cells expressing high levels of *Acta2* and *Col1a1* and much lower levels of *Pdgfra*, *Ly6a*, and *Hic1* (fibrogenic branch). The other was composed of cells that underwent more subtle changes, which may represent activation with incomplete or no differentiation (activated branch; Figure S4C, iii–v).

Clustering of the merged scRNA-seq datasets for *Hic1* CT2 tdTomato⁺ cells before and after damage (Figure S4D) revealed that cFAPs from damaged samples clustered separately from those at a steady state (Figure S4E). Gene Ontology (GO) analysis of the differentially expressed genes in each cluster (Figure S4F) pointed to increased metabolic activity in cluster-2 cells, which we interpreted as a sign of activation, and to upregulation of ECM-associated components as well as pro-angiogenic pathways in cluster-3 cells.

Taken together, these results strongly suggest that, in response to damage, most cFAPs activate, and a subset of them differentiate into fibrogenic cells and downregulate progenitor marker proteins, such as SCA-1 and HIC1.

Inhibition of cFAP Differentiation Improves Cardiac Function

Excessive generation of ECM causes heart-wall stiffening, resulting in impaired cardiac function (Gyöngyösi et al., 2017). We reasoned that inhibiting the differentiation of cFAPs toward SCA-1[−] fibrogenic cells may have a therapeutic effect. We previously identified members of the imatinib/nilotinib tyrosine kinase inhibitor (TKI) family as modulators of FAP survival (Lemos et al., 2015). We found that these compounds were also capable of blocking the upregulation of collagen in TGFβ1-treated cFAPs *in vitro* (Figure 4A). Thus, we investigated whether nilotinib (25 mg/kg/day) could ameliorate ISO-induced cardiac damage. Nilotinib prevented the decrease in the SCA-1⁺/SCA-1[−] ratio

observed with ISO alone (Figure 4B) and significantly reduced fibrotic lesion formation (Figures 4C and 4D), supporting the hypothesis that nilotinib acts, at least in part, by blocking pro-fibrotic differentiation of cFAPs.

As cardiac function was not significantly affected by ISO treatment, we sought to establish the therapeutic potential of blocking cFAP-driven fibrogenesis in the more-severe LAD ligation model. When nilotinib treatment was initiated 2 days before LAD ligation and continued until 4 days after surgery, only 17% of the mice survived in the treated group compared with 100% in the untreated group (Figures 4E and S5). In those mice, the post-MI scar area was smaller and appeared discontinuous, consistent with an inhibition of the initial steps of scar formation (Frantz et al., 2008; Ikeuchi et al., 2004).

To bypass those deleterious effects and to more closely mimic the likely timing of administration of similar drugs to human patients, we initiated the treatment 3 days after surgery and continued for 28 days; after which, cardiac function was assessed.

In vehicle-treated mice, LAD ligation produced a progressive decline in left ventricle (LV) ejection fraction. This was associated with elevated end-diastolic volume (a hallmark of cardiac compromise), as well as increased anterior and posterior LV wall thickness and LV chamber dilation, features of cardiac remodeling (Figure 4F). Interestingly, nilotinib treatment attenuated the decline in ejection fraction and completely prevented the elevation in end-diastolic volume, LV chamber dilation, and LV posterior wall thickening. Similar to the ISO injury model, nilotinib treatment was also associated with a significant increase in the PDGFRα⁺ SCA-1⁺/SCA-1[−] ratio (Figure 4F). Thus, the differentiation step leading to the generation of fibrogenic cells from cFAPs can be pharmacologically targeted to improve post-MI cardiac performance.

A Role for cFAPs in the Pathogenesis of AC

Although adipogenic differentiation of cFAPs was readily observed *in vitro*, their activation after ischemic damage did not lead to the appearance of intramyocardial adipocytes. However, adipocyte accumulation is a well-documented outcome of arrhythmogenic cardiomyopathy (AC), an inherited cardiac disease characterized by replacement of myocardium with fibrofatty deposition leading to life-threatening arrhythmias, especially in young adults (Basso et al., 2009). To confirm the adipogenic potential of cFAPs *in vivo*, we generated a model of that disease by overexpressing human desmoglein 2 (DSG2) carrying a 1672C→T mutation in mice (Pilichou et al., 2006). In AC models, fibrous and/or fatty lesions develop after 9 months of age, and adipocytes have been shown to originate from a

Figure 5. Lineage Tracing of Fibrous/Fatty Depositions in a Murine Model of AC with *Pdgfra* or *Hic1* CT2 Systems

(A) Schematic of the *Pdgfra* CT2 knockin allele. (B–G) Breeding scheme for generation of DSG2^{tmu}/*Pdgfra* CT2 tdTomato (B) or DSG2^{tmu}/*Hic1* CT2 tdTomato (E) mice. Representative images and quantification of the *Pdgfra* CT2 tdTomato⁺ (C) or *Hic1* CT2 tdTomato⁺ cells (F) colocalized with collagen I in fibrous lesions in DSG2^{tmu} mice hearts. A colocalized pixel map image is shown. Line graphs in (C) and (F) represent the intensity profile of tdTomato (red) and collagen I (green) staining across the arrows shown in the merged images; the solid line graphs are for the yellow arrow (no damage), and the broken line graphs are for the white arrow (damaged region; n = 4). Quantification of tdTomato⁺/perilipin⁺ cells (right) and representative images (left) of *Pdgfra* CT2 tdTomato (D) or *Hic1* CT2 tdTomato (G) DSG2^{tmu} whole-heart sections immunostained with perilipin. Higher-magnification images are for areas enclosed by white boxes. 3D reconstruction of the z stack of the area enclosed by the blue box is shown in (D). n = 4 for *Hic1*-traced cells; n = 6 for *Pdgfra*-traced cells. Data in the graphs in Figure 5 are represented as means ± SEM. *p < 0.05 compared with other groups.

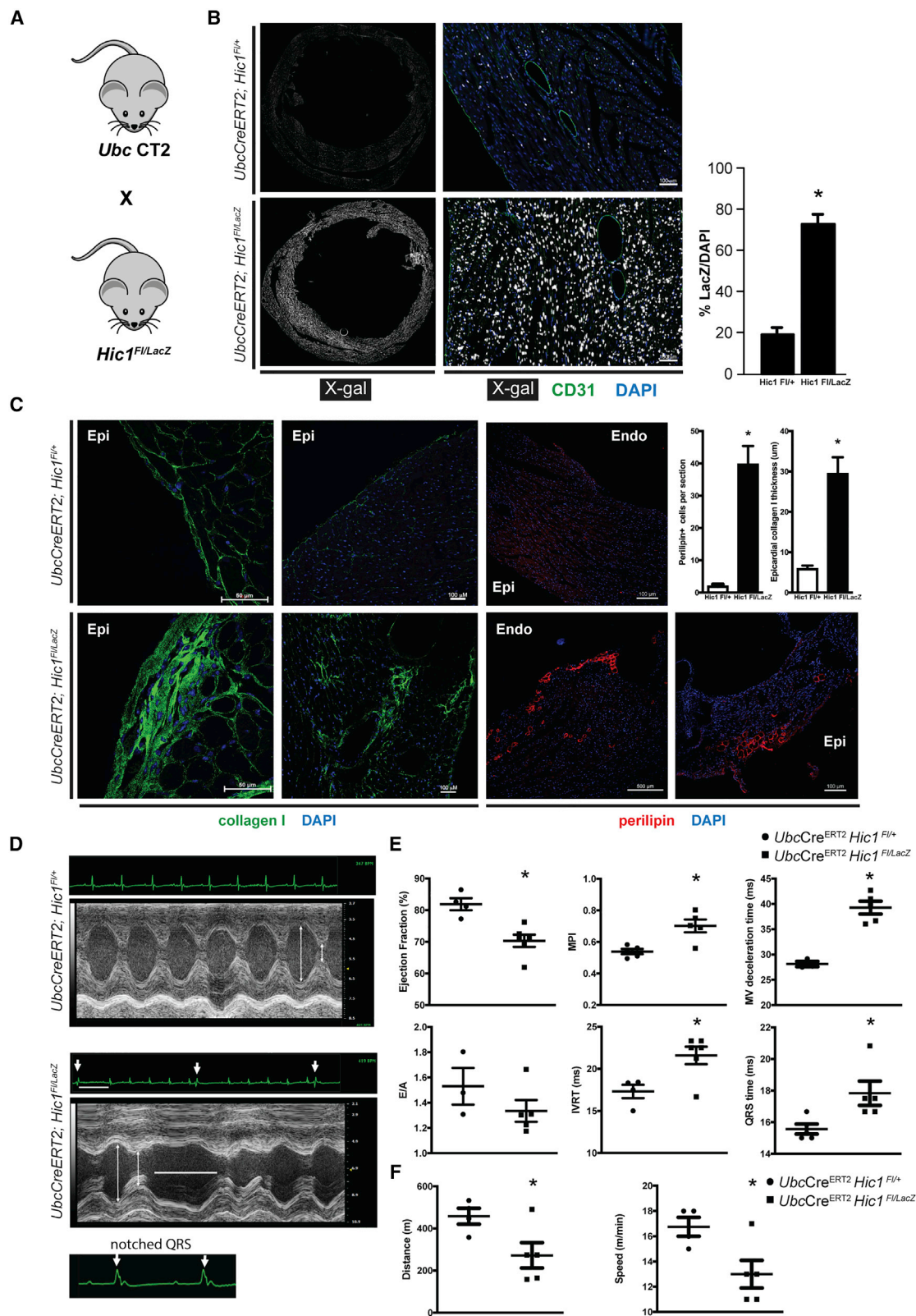


Figure 6. *Hic1* Deletion Leads to Activation of cFAPs and AC-like Phenotype in the Absence of Overt Cardiomyocyte Damage

(A) Breeding scheme for generating *Ubc CT2 Hic1^{F/LacZ}* mice.

(B) Representative images and quantification of the X-gal⁺ cells in *Ubc CT2 Hic1^{F/LacZ}* mice hearts 10 days after TAM (n = 5).

(legend continued on next page)

Pdgfra⁺ precursor. However, as a non-inducible *Pdgfra*-Cre was used, it was unclear whether expression of that marker took place during development or in the adult heart (Lombardi et al., 2016). To assess whether such infiltrations originate from *Hic1*⁺ cells, we bred the tdTomato reporter and either the *Hic1*-CT2 or the *Pdgfra*-CT2 transgenes into that strain (Figures 5A, 5B, and 5E). We first confirmed that pre-existing adipocytes, such as those found in pericardial fat, were not labeled with tdTomato in either lineage-tracing systems (Figures S6A and S6B). In the AC model, consistent with the ischemic injury models, *Hic1*- or *Pdgfra*-traced cells were enriched in areas of collagen deposition (Figures 5C and 5F). In addition, most intramyocardial adipocytes were tdTomato⁺ (Figures 5D, 5G, S6C, and S6D) confirming that *Pdgfra*⁺ *Hic1*⁺ progenitors are adipogenic *in vivo* and are the origin of fibrofatty depositions in AC.

***Hic1* Deletion Leads to Development of AC-like Pathology in the Absence of Cardiomyocyte Damage**

The lack of adipocytic infiltrations in ischemic damage and their abundance in DSG2 mutant mice suggests that the differentiated output of cFAPs is influenced by the type of injury. Next, we sought to assess their *in vivo* lineage potential in the absence of any overt (LAD ligation) or subclinical (AC) damage. We recently found that HIC1 regulates mesenchymal progenitor quiescence (Scott et al., 2019) and that its deletion leads to spontaneous FAP activation in multiple tissues. Indeed, in *Ubc*-CT2 *Hic1*^{FII/LacZ} mice (Figure 6A), TAM treatment, resulting in a decrease of *Hic1* expression by 89.4%, led to a marked increase of LacZ⁺ cells within 10 days (Figure 6B). *Hic1* conditional knockout (cKO) hearts showed marked epicardial thickening and/or interstitial fibrosis as well as intramyocardial adipocytes at 6 months to 1 year after TAM treatment (Figure 6C). In those mice, cardiac function was compromised, as illustrated by reduced LV ejection fraction as well as increased myocardial performance index (MPI), isovolumic relaxation time (IVRT), and mitral valve (MV) deceleration time (Figures 6D and 6E). Additionally, electrocardiogram (ECG) tracings showed arrhythmias in the form of premature ventricular contractions as well as notched QRS complexes (30% of tested animals; white arrows in Figure 6D), which are sometimes associated with interstitial fibrosis (Kawasaki et al., 2015). To evaluate the systemic effects of these changes, we subjected those mice to forced exercise and assessed their endurance. The distance and speed reached until fatigue were significantly lower in *Hic1* cKO mice compared with control mice (Figure 6F).

The *Ubc*-CT2 *Hic1*^{FII/LacZ} leads to near ubiquitous deletion of *Hic1*, preventing us from attributing the observed phenotype to cFAPs. To circumvent this confounding factor, we bred *Hic1*^{FII/FI} mice with *Pdgfra* CT2 tdTomato mice (which led to

a decrease in *Hic1* expression by 85.2%; Figure 7A) and confirmed that most cells composing the fibrous and fatty lesions originated from *Pdgfra*⁺ cells (Figure 7B). As expected, those mice developed signs of cardiac dysfunction (Figures 7C and 7D) comparable to those described above. To further explore whether *Hic1* may be a modifier of the penetrance of AC, we crossed the DSG2^{mu} mice with *Pdgfra* CT2 *Hic1*^{FII/FI} mice and compared them to their parental strains. At 6 months of age and 1 month after TAM, intramyocardial adipocytes were limited in the DSG2^{mu} mice (as at that age, DSG2^{mu} mice do not display overt lesions yet) and were significantly increased in the other two strains. Interestingly, mice harboring both the DSG2 mutation and the *Hic1* cKO allele exhibited approximately double the number of adipocytes present as those in the *Hic1* cKO mice (Figure 7E). Thus, damage-independent activation of cFAPs leads to fibrous/fatty lesions and arrhythmias reminiscent of human AC even in the absence of cardiac damage and accelerates fat deposition in the presence of subclinical damage, underpinning the key role of those cells in AC pathophysiology.

DISCUSSION

The cellular mechanisms leading to cardiac fibrosis and fatty degeneration remain poorly understood. During the past several years, various markers have been proposed to identify cardiac fibroblasts, such as *Pdgfra*, *Tcf21*, and *Col1a1*. However, despite reports that multipotent progenitors are also contained within those populations (Chong et al., 2011), their phenotypic heterogeneity and functional properties have not been explored in depth.

Here, we show that a significant portion of the PDGFRa⁺ cells form colonies *in vitro* and represent mesenchymal progenitors with fibro-adipogenic potential and that this subpopulation is characterized by expression of *Ly6a*/*Sca-1* and *Hic1*. We further show that such potential is also expressed *in vivo*. In skeletal muscle, FAPs can also respond to exogenous BMPs or pathogenic alterations to generate ectopic bone (Wosczyzna et al., 2012), suggesting that the recently reported osteogenic potential of cardiac fibroblasts (Pillai et al., 2017) may, at least in part, reside within that population.

Our lineage-tracing experiments excluded any significant contribution of *Pdgfra*⁺ or *Hic1*⁺ cells to cardiomyocytes or endothelial cells, either spontaneously or after damage. Thus, unlike what was previously described for mesenchymal stem cells (Noseda et al., 2015; Ubil et al., 2014), their potential is restricted to connective tissue elements.

Previous publications found little evidence of contribution of *Sca-1* lineage-traced cells to the scar. However, caveats of those analyses are the strong expression of *Ly6a* in endothelial

(C) Representative images showing epicardial and interstitial fibrosis and perilipin⁺ adipocytes in *Hic1*-deleted mice hearts 1 year after TAM (Epi, epicardial side; Endo, endocardial side). (Top right) Quantification of the epicardial-layer thickness and perilipin⁺ cells/section (n = 3 in the *Hic1*^{FII/+}; n = 5 in *Hic1*^{FII/FI} group).

(D) Representative M-mode echo and ECG tracings of *Ubc* CT2 *Hic1*^{FII/LacZ} mice hearts. White arrows and horizontal lines highlight the premature ventricular extra beats and associated refractory pause, respectively. White arrowheads highlight notched QRS complexes found in *Hic1* cKO mice.

(E) Quantification of cardiac function in *Hic1* cKO mice and their controls. Ejection fraction, myocardial performance index (MPI), E/A ratio, isovolumic relaxation time (IVRT), and mitral valve (MV) deceleration time were calculated to determine systolic and diastolic function. QRS time was determined from the ECG tracings during the echo procedure (n = 4 for *Hic1*^{FII/+} group; n = 6 for *Hic1*^{FII/LacZ} group).

(F) Quantification of the speed and distance reached by mice force-exercised on a treadmill as indices of physical endurance in *Hic1* cKO mice (n = 4 for *Hic1*^{FII/+}; n = 5 for *Hic1*^{FII/FI} group).

Data in the graphs in Figure 6 are represented as means ± SEM. *p < 0.05 compared with other groups.

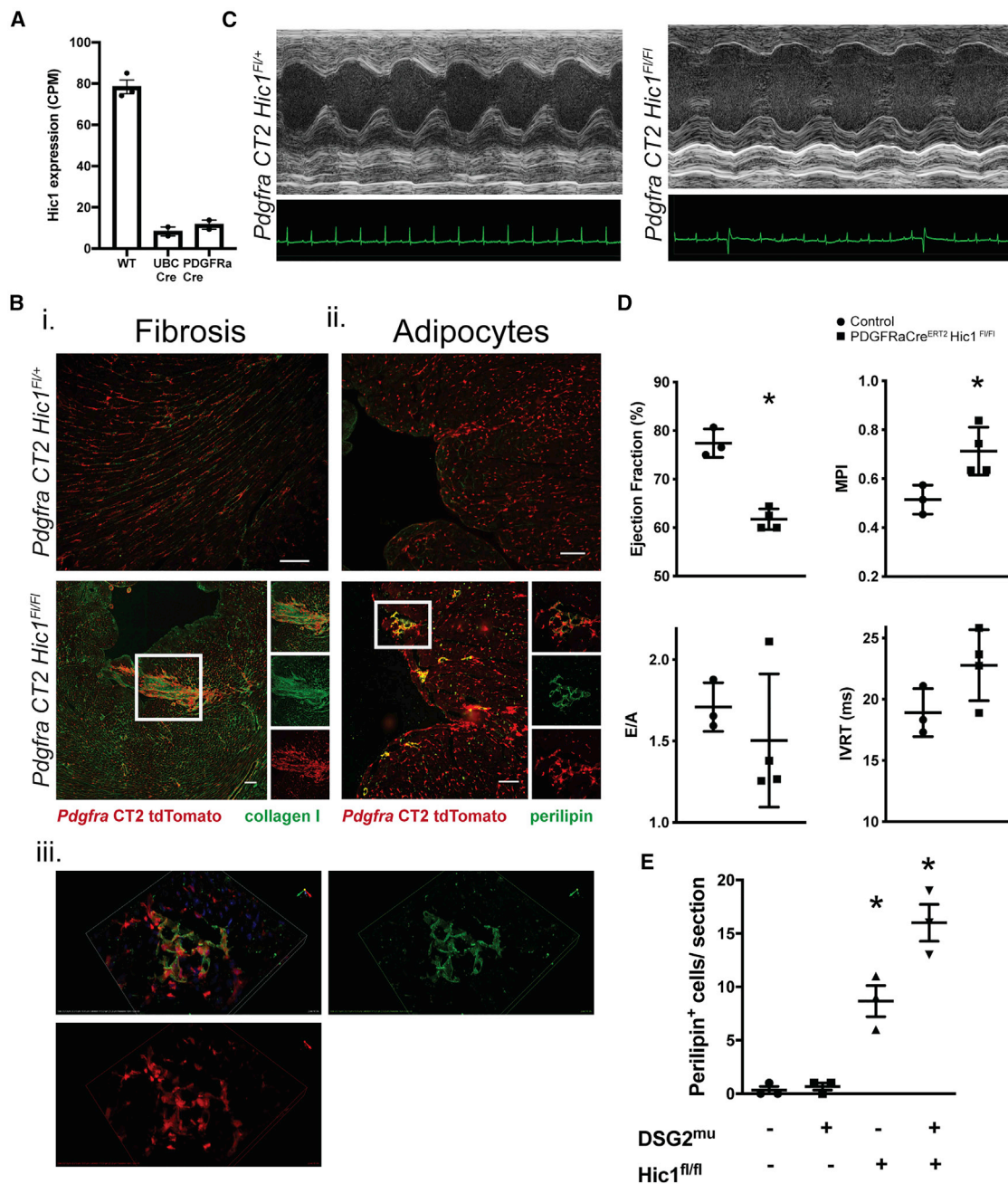


Figure 7. The AC-like Phenotype Induced by *Hic1* Deletion Is Attributable to *Pdgfra*-Labeled Cells

(A) *Hic1* RNA expression in wild-type (WT), *Ubc CT2 Hic1^{F/F}*, and *Pdgfra CT2 Hic1^{F/F}* as a measure of Cre efficiency. (B) Representative images showing fibrosis (i) and perilipin⁺ adipocyte infiltrations (ii) in *Pdgfra CT2 Hic1^{F/F}* hearts 2 months after TAM (scale bar: 100 μ m); (iii) 3D reconstruction of the z stack of the adipocyte cluster in the white box in (ii). (C) Representative M-mode echo and ECG tracings of *Pdgfra CT2 Hic1^{F/F}* mice hearts. (D) Quantification of ejection fraction, MPI, E/A ratio, and IVRT in *Pdgfra CT2 Hic1^{F/F}* mice hearts (n = 3 for control; 4 for *Pdgfra CT2 Hic1^{F/F}*). (E) Quantification of perilipin⁺ cells in DSG2^{mu}/*Pdgfra CT2 Hic1^{F/F}* mice heart sections and their parental strains (n = 3). Data in the graphs in Figure 7 are represented as means \pm SEM. *p < 0.05 compared with other groups.

cells, relative to stromal cells, and the consequent poor recombination efficiency in the stroma, reported to be as low as 9%–13% (Neidig et al., 2018; Vagnozzi et al., 2018). In fact, despite the poor recombination efficiency of *Ly6a*-Cre, contribution of the PDGFRa⁺/SCA-1⁺ cells to scar formation post-MI has

recently been documented, strongly supporting our findings (Tang et al., 2018).

Here, we show that *Hic1*-driven CT2 marks a subpopulation within *Pdgfra*-expressing cells. In view of their predominant fates *in vitro* and *in vivo*, and in keeping with the nomenclature in use

in skeletal muscle, we propose that PDGFRa⁺, SCA-1⁺, HIC1⁺ positive cells be called “cardiac fibro/adipogenic progenitors (cFAPs)” as used in this study.

We identify a differentiation hierarchy within cardiac PDGFRa⁺ cells, with cFAPs consistently generating a small number of SCA-1⁺-differentiated cells in the undamaged heart. A caveat to that interpretation lies in the fact that TAM treatment may be cardiotoxic (Bersell et al., 2013). At homeostasis, both cFAPs and their progeny express low levels of ECM genes. After damage, however, those genes are highly upregulated, specifically in the differentiated SCA-1⁺ cells. Eventually, such a fibrogenic transcriptional program is gradually downregulated to the point at which little difference remains between SCA-1⁺ progenitors and SCA-1⁺ progeny at 1 month after injury. This validates the proposed existence of cardiac fibroblasts in at least two states: deactivated and active. In addition, the persistence of SCA-1⁺, deactivated cells in the damaged area indicates that the gene-expression changes triggered by damage are not fully reversible, suggesting differentiation has taken place, as opposed to a temporary change in functional state.

Inhibition of cFAP differentiation step using nilotinib, a second-generation TKI, led to an improvement of heart function after an infarction and reduced the generation of SCA-1⁺ cells from cFAPs. Consistent with those results, imatinib, an earlier member of the same TKI family, was shown to also have favorable effects on rat cardiac function post-MI (Liu et al., 2014). It is likely that these kinase inhibitors, which have among their targets important proteins involved in fibrosis, such as *Pdgfra*, may exert their effects by acting on multiple biological processes. Here, we provide clear evidence that one such process is the generation of fibrogenic cells from tissue-resident multipotent progenitors. Although our experiments provide proof of principle that modulation of cFAP differentiation is a viable therapeutic strategy, the reported cardiotoxicity of nilotinib (Moslehi and Deininger, 2015) raises questions about whether its long-term use in infarct patients is appropriate and provides a strong rationale for testing alternative TKIs.

By performing lineage tracing in a mouse model of AC, we show that the *Hic1*⁺ subset of *Pdgfra*⁺ cells are responsible for the generation of the intramyocardial adipocytes pathognomonic of that disease. This is in stark contrast with those cells' exclusive generation of more-fibrogenic progeny in the context of myocardial infarction, suggesting that the extent and/or nature of damage is likely to influence their lineage choice, possibly through the upregulation of known anti-adipogenic factors, such as TGF- β and Wnts (Blankesteijn et al., 2000; Deten et al., 2001).

Quiescence of stromal progenitors can be disrupted by deleting *Hic1*, a transcriptional repressor that modulates the expression of cell-cycle genes (Scott et al., 2019). In the heart, this led to a rapid increase in LacZ⁺ cells, followed by the slower appearance of intramyocardial adipocytes and fibrosis and eventually to clinical signs reminiscent of human AC. This suggests that the main effect of the desmosomal mutations linked to AC may be to cause the chronic activation of stromal progenitors, including cFAPs, which represents the key pathologic event.

Our work reveals that significant proportions of cells meeting the phenotypic definition of cardiac fibroblasts are actually multipotent progenitors and supports a fundamental contribution of those cells to human AC pathology. It also suggests that after ischemic damage, TKIs can be used to modulate the appear-

ance of fibrogenic cells with positive results on cardiac performance, providing a rationale for exploring a different therapeutic approach for one of the most common and debilitating diseases of our time.

STAR★METHODS

Detailed methods are provided in the online version of this paper and include the following:

- KEY RESOURCES TABLE
- LEAD CONTACT AND MATERIALS AVAILABILITY
- EXPERIMENTAL MODEL AND SUBJECT DETAILS
 - Mice
 - FAP primary culture
- METHOD DETAILS
 - Induction of cardiac damage and Nilotinib treatment
 - Heart digestion and fluorescence-activated cell sorting (FACS)
 - Analysis of FAP proliferation
 - *in situ* X-gal staining and immunofluorescence/histology
 - Image acquisition and quantification
 - Echocardiography
 - Treadmill forced exercise test
 - Quantitative Reverse Transcription PCR
 - Gene expression profiling – popRNA-seq
 - RNA-seq Bioinformatic Analyses
 - Single Cell RNA-seq
- QUANTIFICATION AND STATISTICAL ANALYSIS
- DATA AND CODE AVAILABILITY

SUPPLEMENTAL INFORMATION

Supplemental Information can be found online at <https://doi.org/10.1016/j.stem.2019.12.008>.

ACKNOWLEDGMENTS

This work was supported by Canadian Institutes of Health Research (grant FDN-159908) and the Heart and Stroke Foundation of Canada (grant G-19-0026541 to F.M.V.R. and PJT-149026 and PJT-148816 to T.M.U.), a Terry Fox New Frontiers Program (project grant 1021 to T.M.U.), and National Institutes of Health (grant CA231652 to T.M.U.). M.A. was supported by a University of British Columbia graduate scholarship. We thank Erwan Le Neve, Lochlan Fisher, Mariam Hammoud, and Ingrid Barta for technical assistance, as well as the BRC-seq, UBC FACS, AbLab, and BRC genotyping and transgenic units.

AUTHOR CONTRIBUTIONS

H.S., B.P., R.W.S., D.R.L., C.C., M.A., M.L., C.L., and D.F. were responsible for performing all experiments. H.S., B.P., R.W.S., F.M.V.R., and T.M.U. were involved in experimental design, data interpretation, and preparation of the manuscript. All authors were involved in editing the manuscript.

DECLARATION OF INTERESTS

The authors have no competing interests.

Received: November 2, 2018

Revised: October 2, 2019

Accepted: December 18, 2019

Published: January 23, 2020; corrected online: February 12, 2020

REFERENCES

- Basso, C., Corrado, D., Marcus, F.I., Nava, A., and Thiene, G. (2009). Arrhythmogenic right ventricular cardiomyopathy. *Lancet* 373, 1289–1300.
- Bersell, K., Choudhury, S., Mollova, M., Polizzotti, B.D., Ganapathy, B., Walsh, S., Wadugu, B., Arab, S., and Kühn, B. (2013). Moderate and high amounts of tamoxifen in α MHC-MerCreMer mice induce a DNA damage response, leading to heart failure and death. *Dis. Model. Mech.* 6, 1459–1469.
- Blankesteijn, W.M., van Gijn, M.E., Essers-Janssen, Y.P., Daemen, M.J., and Smits, J.F. (2000). Beta-catenin, an inducer of uncontrolled cell proliferation and migration in malignancies, is localized in the cytoplasm of vascular endothelium during neovascularization after myocardial infarction. *Am. J. Pathol.* 157, 877–883.
- Bostick, B., Shin, J.-H., Yue, Y., Wasala, N.B., Lai, Y., and Duan, D. (2012). AAV micro-dystrophin gene therapy alleviates stress-induced cardiac death but not myocardial fibrosis in >21-m-old mdx mice, an end-stage model of Duchenne muscular dystrophy cardiomyopathy. *J. Mol. Cell. Cardiol.* 53, 217–222.
- Chong, J.J.H., Chandrakanthan, V., Xaymardan, M., Asli, N.S., Li, J., Ahmed, I., Heffernan, C., Menon, M.K., Scarlett, C.J., Rashidianfar, A., et al. (2011). Adult cardiac-resident MSC-like stem cells with a proepicardial origin. *Cell Stem Cell* 9, 527–540.
- Chun, J.L., O'Brien, R., Song, M.H., Wondrasch, B.F., and Berry, S.E. (2013). Injection of vessel-derived stem cells prevents dilated cardiomyopathy and promotes angiogenesis and endogenous cardiac stem cell proliferation in mdx/utrn^{-/-} but not aged mdx mouse models for duchenne muscular dystrophy. *Stem Cells Transl. Med.* 2, 68–80.
- Chung, M.I., Bujnis, M., Barkauskas, C.E., Kobayashi, Y., and Hogan, B.L.M. (2018). Niche-mediated BMP/SMAD signaling regulates lung alveolar stem cell proliferation and differentiation. *Development* 145, dev163014.
- Deten, A., Hölzl, A., Leicht, M., Barth, W., and Zimmer, H.-G. (2001). Changes in extracellular matrix and in transforming growth factor beta isoforms after coronary artery ligation in rats. *J. Mol. Cell. Cardiol.* 33, 1191–1207.
- Dobin, A., Davis, C.A., Schlesinger, F., Drenkow, J., Zaleski, C., Jha, S., Batut, P., Chaisson, M., and Gingeras, T.R. (2013). STAR: ultrafast universal RNA-seq aligner. *Bioinformatics* 29, 15–21.
- Farbehi, N., Patrick, R., Dorison, A., Xaymardan, M., Janbandhu, V., Wystub-Lis, K., Ho, J.W.K., Nordon, R.E., and Harvey, R.P. (2019). Single-cell expression profiling reveals dynamic flux of cardiac stromal, vascular and immune cells in health and injury. *eLife* 8, e43882.
- Festa, E., Fretz, J., Berry, R., Schmidt, B., Rodeheffer, M., Horowitz, M., and Horsley, V. (2011). Adipocyte lineage cells contribute to the skin stem cell niche to drive hair cycling. *Cell* 146, 761–771.
- Frangogiannis, N.G. (2012). Matricellular proteins in cardiac adaptation and disease. *Physiol. Rev.* 92, 635–688.
- Frantz, S., Hu, K., Adamek, A., Wolf, J., Sallam, A., Maier, S.K., Lonning, S., Ling, H., Ertl, G., and Bauersachs, J. (2008). Transforming growth factor beta inhibition increases mortality and left ventricular dilatation after myocardial infarction. *Basic Res. Cardiol.* 103, 485–492.
- Gyöngyösi, M., Winkler, J., Ramos, I., Do, Q.-T., Firat, H., McDonald, K., González, A., Thum, T., Díez, J., Jaisser, F., et al. (2017). Myocardial fibrosis: biomedical research from bench to bedside. *Eur. J. Heart Fail.* 19, 177–191.
- Hamilton, T.G., Klinghoffer, R.A., Corrin, P.D., and Soriano, P. (2003). Evolutionary divergence of platelet-derived growth factor alpha receptor signaling mechanisms. *Mol. Cell. Biol.* 23, 4013–4025.
- Haniffa, M.A., Collin, M.P., Buckley, C.D., and Dazzi, F. (2009). Mesenchymal stem cells: the fibroblasts' new clothes? *Haematologica* 94, 258–263.
- Heather, L.C., Catchpole, A.F., Stuckey, D.J., Cole, M.A., Carr, C.A., and Clarke, K. (2009). Isoproterenol induces in vivo functional and metabolic abnormalities: similar to those found in the infarcted rat heart. *J. Physiol. Pharmacol.* 60, 31–39.
- Hematti, P. (2012). Mesenchymal stromal cells and fibroblasts: a case of mistaken identity? *Cytotherapy* 14, 516–521.
- Huang, W., Sherman, B.T., and Lempicki, R.A. (2009a). Bioinformatics enrichment tools: paths toward the comprehensive functional analysis of large gene lists. *Nucleic Acids Res.* 37, 1–13.
- Huang, W., Sherman, B.T., and Lempicki, R.A. (2009b). Systematic and integrative analysis of large gene lists using DAVID bioinformatics resources. *Nat. Protoc.* 4, 44–57.
- Ieronimakis, N., Hays, A.L., Janebodan, K., Mahoney, W.M., Jr., Duffield, J.S., Majesky, M.W., and Reyes, M. (2013). Coronary adventitial cells are linked to perivascular cardiac fibrosis via TGF β 1 signaling in the mdx mouse model of Duchenne muscular dystrophy. *J. Mol. Cell. Cardiol.* 63, 122–134.
- Ikeuchi, M., Tsutsui, H., Shiomi, T., Matsusaka, H., Matsushima, S., Wen, J., Kubota, T., and Takeshita, A. (2004). Inhibition of TGF- β signaling exacerbates early cardiac dysfunction but prevents late remodeling after infarction. *Cardiovasc. Res.* 64, 526–535.
- Joe, A.W.B., Yi, L., Natarajan, A., Le Grand, F., So, L., Wang, J., Rudnicki, M.A., and Rossi, F.M.V. (2010). Muscle injury activates resident fibro/adipogenic progenitors that facilitate myogenesis. *Nat. Cell Biol.* 12, 153–163.
- Kalajic, I., Kalajic, Z., Kaliterna, M., Gronowicz, G., Clark, S.H., Lichter, A.C., and Rowe, D. (2002). Use of type I collagen green fluorescent protein transgenes to identify subpopulations of cells at different stages of the osteoblast lineage. *J. Bone Miner. Res.* 17, 15–25.
- Kanickak, O., Khalil, H., Ivey, M.J., Karch, J., Maliken, B.D., Correll, R.N., Brody, M.J., J. Lin, S.C., Aronow, B.J., Tallquist, M.D., and Molkentin, J.D. (2016). Genetic lineage tracing defines myofibroblast origin and function in the injured heart. *Nat. Commun.* 7, 12260.
- Kawasaki, T., Harimoto, K., Honda, S., Sato, Y., Yamano, M., Miki, S., and Kamitani, T. (2015). Notched QRS for the assessment of myocardial fibrosis in hypertrophic cardiomyopathy. *Circ. J.* 79, 847–853.
- Kolk, M.V.V., Meyberg, D., Deuse, T., Tang-Quan, K.R., Robbins, R.C., Reichenspurner, H., and Schrepfer, S. (2009). LAD-ligation: a murine model of myocardial infarction. *J. Vis. Exp.* (32), 1438.
- Langmead, B., and Salzberg, S.L. (2012). Fast gapped-read alignment with Bowtie 2. *Nat. Methods* 9, 357–359.
- Lemos, D.R., Babaeijandaghi, F., Low, M., Chang, C.-K., Lee, S.T., Fiore, D., Zhang, R.-H., Natarajan, A., Nedospasov, S.A., and Rossi, F.M.V. (2015). Nilotinib reduces muscle fibrosis in chronic muscle injury by promoting TNF-mediated apoptosis of fibro/adipogenic progenitors. *Nat. Med.* 21, 786–794.
- Liu, C., Zhao, W., Meng, W., Zhao, T., Chen, Y., Ahokas, R.A., Liu, H., and Sun, Y. (2014). Platelet-derived growth factor blockade on cardiac remodeling following infarction. *Mol. Cell. Biochem.* 397, 295–304.
- Lombardi, R., Chen, S.N., Ruggiero, A., Gurha, P., Czernuszewicz, G.Z., Willerson, J.T., and Marian, A.J. (2016). Cardiac fibro-adipocyte progenitors express desmosome proteins and preferentially differentiate to adipocytes upon deletion of the desmoplakin gene. *Circ. Res.* 119, 41–54.
- Merrick, D., Sakers, A., Irgebay, Z., Okada, C., Calvert, C., Morley, M.P., Percec, I., and Seale, P. (2019). Identification of a mesenchymal progenitor cell hierarchy in adipose tissue. *Science* 364, eaav2501.
- Moslehi, J.J., and Deininger, M. (2015). Tyrosine kinase inhibitor-associated cardiovascular toxicity in chronic myeloid leukemia. *J. Clin. Oncol.* 33, 4210–4218.
- Neidig, L.E., Weinberger, F., Palpant, N.J., Mignone, J., Martinson, A.M., Sorensen, D.W., Bender, I., Nemoto, N., Reinecke, H., Pabon, L., et al. (2018). Evidence for minimal cardiogenic potential of stem cell antigen 1-positive cells in the adult mouse heart. *Circulation* 138, 2960–2962.
- Noseda, M., Harada, M., McSweeney, S., Leja, T., Belian, E., Stuckey, D.J., Abreu Paiva, M.S., Habib, J., Macaulay, I., de Smith, A.J., et al. (2015). PDGFR α demarcates the cardiogenic clonogenic Sca1⁺ stem/progenitor cell in adult murine myocardium. *Nat. Commun.* 6, 6930.
- Pelekanos, R.A., Li, J., Gongora, M., Chandrakanthan, V., Scown, J., Suhaimi, N., Brooke, G., Christensen, M.E., Doan, T., Rice, A.M., et al. (2012). Comprehensive transcriptome and immunophenotype analysis of renal and cardiac MSC-like populations supports strong congruence with bone marrow MSC despite maintenance of distinct identities. *Stem Cell Res. (Amst.)* 8, 58–73.

- Pilichou, K., Nava, A., Basso, C., Beffagna, G., Baucé, B., Lorenzon, A., Frigo, G., Vettori, A., Valente, M., Towbin, J., et al. (2006). Mutations in desmoglein-2 gene are associated with arrhythmogenic right ventricular cardiomyopathy. *Circulation* 113, 1171–1179.
- Pillai, I.C.L., Li, S., Romay, M., Lam, L., Lu, Y., Huang, J., Dillard, N., Zemanova, M., Rubbi, L., Wang, Y., et al. (2017). Cardiac fibroblasts adopt osteogenic fates and can be targeted to attenuate pathological heart calcification. *Cell Stem Cell* 20, 218–232.e5.
- Pinto, A.R., Illykh, A., Ivey, M.J., Kuwabara, J.T., D'Antoni, M.L., Debuque, R., Chandran, A., Wang, L., Arora, K., Rosenthal, N.A., and Tallquist, M.D. (2016). Revisiting cardiac cellular composition. *Circ. Res.* 118, 400–409.
- Pospichalova, V., Tureckova, J., Faflek, B., Vojtechova, M., Krausova, M., Lukas, J., Sloncova, E., Takacova, S., Divoky, V., Leprince, D., et al. (2011). Generation of two modified mouse alleles of the Hic1 tumor suppressor gene. *Genesis* 49, 142–151.
- Satija, R., Farrell, J.A., Gennert, D., Schier, A.F., and Regev, A. (2015). Spatial reconstruction of single-cell gene expression data. *Nat. Biotechnol.* 33, 495–502.
- Schindelin, J., Arganda-Carreras, I., Frise, E., Kaynig, V., Longair, M., Pietzsch, T., Preibisch, S., Rueden, C., Saalfeld, S., Schmid, B., et al. (2012). Fiji: an open-source platform for biological-image analysis. *Nat. Methods* 9, 676–682.
- Scott, R.W., Arostegui, M., Schweitzer, R., Rossi, F.M.V., and Underhill, T.M. (2019). Hic1 Defines Quiescent Mesenchymal Progenitor Subpopulations with Distinct Functions and Fates in Skeletal Muscle Regeneration. *Cell Stem Cell* 25, 797–813.e9.
- See, F., Kompa, A., Martin, J., Lewis, D.A., and Krum, H. (2005). Fibrosis as a therapeutic target post-myocardial infarction. *Curr. Pharm. Des.* 11, 477–487.
- Skelly, D.A., Squiers, G.T., McLellan, M.A., Bolisetty, M.T., Robson, P., Rosenthal, N.A., and Pinto, A.R. (2018). Single-cell transcriptional profiling reveals cellular diversity and intercommunication in the mouse heart. *Cell Rep.* 22, 600–610.
- Stuart, T., Butler, A., Hoffman, P., Hafemeister, C., Papalexi, E., Mauck, W.M., 3rd, Hao, Y., Stoeckius, M., Smibert, P., and Satija, R. (2019). Comprehensive Integration of Single-Cell Data. *Cell* 177, 1888–1902.e21.
- Tang, J., Li, Y., Huang, X., He, L., Zhang, L., Wang, H., Yu, W., Pu, W., Tian, X., Nie, Y., et al. (2018). Fate Mapping of Sca1⁺ cardiac progenitor cells in the adult mouse heart. *Circulation* 138, 2967–2969.
- Trapnell, C., Williams, B.A., Pertea, G., Mortazavi, A., Kwan, G., van Baren, M.J., Salzberg, S.L., Wold, B.J., and Pachter, L. (2010). Transcript assembly and quantification by RNA-Seq reveals unannotated transcripts and isoform switching during cell differentiation. *Nat. Biotechnol.* 28, 511–515.
- Trapnell, C., Cacchiarelli, D., Grimsby, J., Pokharel, P., Li, S., Morse, M., Lennon, N.J., Livak, K.J., Mikkelsen, T.S., and Rinn, J.L. (2014). The dynamics and regulators of cell fate decisions are revealed by pseudotemporal ordering of single cells. *Nat. Biotechnol.* 32, 381–386.
- Ubil, E., Duan, J., Pillai, I.C.L., Rosa-Garrido, M., Wu, Y., Bargiacchi, F., Lu, Y., Stanboul, S., Huang, J., Rojas, M., et al. (2014). Mesenchymal-endothelial transition contributes to cardiac neovascularization. *Nature* 514, 585–590.
- Uezumi, A., Fukada, S., Yamamoto, N., Takeda, S., and Tsuchida, K. (2010). Mesenchymal progenitors distinct from satellite cells contribute to ectopic fat cell formation in skeletal muscle. *Nat. Cell Biol.* 12, 143–152.
- Vagnozzi, R.J., Sargent, M.A., Lin, S.J., Palpant, N.J., Murry, C.E., and Molkentin, J.D. (2018). Genetic lineage tracing of Sca-1⁺ cells reveals endothelial but not myogenic contribution to the murine heart. *Circulation* 138, 2931–2939.
- Wosczyzna, M.N., Biswas, A.A., Cogswell, C.A., and Goldhamer, D.J. (2012). Multipotent progenitors resident in the skeletal muscle interstitium exhibit robust BMP-dependent osteogenic activity and mediate heterotopic ossification. *J. Bone Miner. Res.* 27, 1004–1017.
- Younes, H., Möller, T., Lorincz, M.C., Karimi, M.M., and Jones, S.J. (2015). VisRseq: R-based visual framework for analysis of sequencing data. *BMC Bioinformatics* 16 (Suppl 11), S2.

STAR★METHODS

KEY RESOURCES TABLE

REAGENT or RESOURCE	SOURCE	IDENTIFIER
Antibodies		
Rat anti-Ly-6A/E (Sca-1) unconjugated	eBioscience	Cat# 14-5981-82; RRID: AB_467778; clone D7
Rabbit anti-Collagen I polyclonal	Bio Rad	Cat# 2150-1410; RRID: AB_620433
Mouse anti-Collagen I	Abcam	Cat# ab90395; RRID: AB_2049527; Clone COL-1
Rabbit anti-perilipin A/B	Millipore Sigma	Sigma-Aldrich Cat# P1873; RRID: AB_532267
Rat anti-CD31	Bd Bioscience	Cat# 550274; RRID: AB_393571; Clone MEC 13.3
Rabbit anti-NG2 polyclonal	Abcam	Cat# ab129051
Goat anti-PDGFRa polyclonal	R&D	Cat# AF1062; RRID: AB_2236897
Alexa Fluor 488 goat anti-mouse IgG (H+L)	ThermoFisher	Cat# A11029; RRID: AB_2534088
Alexa Fluor 488 goat anti-rabbit IgG (H+L)	ThermoFisher	Cat# A11034; RRID: AB_2576217
Alexa Fluor 488 goat anti-rat IgG (H+L)	ThermoFisher	Cat # A-11006; RRID: AB_2534074
Alexa Fluor 488 donkey anti-goat IgG (H+L)	ThermoFisher	Cat # A-11055; RRID: AB_2534102
Alexa Fluor 555 goat anti-rat IgG (H+L)	ThermoFisher	Cat# A21434; RRID: AB_2535855
Alexa Fluor 555 goat anti-rabbit IgG (H+L)	ThermoFisher	Cat # A21428; RRID: AB_2535849
Alexa Fluor 555 donkey anti-goat IgG (H+L)	ThermoFisher	Cat # A-21432; RRID: AB_2535853
Alexa Fluor 647 goat anti-rat IgG (H+L)	ThermoFisher	Cat# A21247; RRID: AB_141778
Alexa Fluor 647 goat anti-rabbit IgG (H+L)	ThermoFisher	Cat# A21245; RRID: AB_2535813
Alexa Fluor 647 goat anti-mouse IgG (H+L)	ThermoFisher	Cat# A-21235; RRID: AB_2535804
Alexa Fluor 647 donkey anti-rat IgG (H+L)	Southern Biotech	Cat# 6430-31; RRID: AB_2796358
PE-Cy7 anti-Ly-6A/E (Sca-1)	eBioscience	Cat# 25-5981-82; RRID: AB_469669; clone D7
anti-CD31-FITC	eBioscience	Cat# 11-0311-85; RRID: AB_465013; clone MEC 13.3
anti-CD31-APC	BD Biosciences	Cat# 551262; RRID: AB_398497; clone MEC 13.3
anti-panCD45-Alexa 647	UBC Ablab	Cat# 67-0047-01; clone 13/2
anti-CD45.2-FITC	eBioscience	Cat# 11-0454-85; RRID: AB_465062
anti-PDGFRa-APC	BD Biosciences	Cat# 562777; RRID: AB_2737788; clone APA5
APC anti-mouse CD146 Antibody	Biolegend	Cat# 134712; RRID: AB_2563088; clone ME-9F1
PE-Cy7 anti-mouse CD146 Antibody	Biolegend	Cat# 134714; RRID: AB_2563109; clone ME-9F1
TotalSeq A0301 hashtag 1	Biolegend	Cat# 155801; RRID: AB_2750032; M1/42; 30-F11
TotalSeq A0302 hashtag 2	Biolegend	Cat# 155803; RRID: AB_2750033; M1/42; 30-F11
TotalSeq A0303 hashtag 3	Biolegend	Cat# 155805; RRID: AB_2750034; M1/42; 30-F11
TotalSeq A0304 hashtag 4	Biolegend	Cat# 155807; RRID: AB_2750035; M1/42; 30-F11
Chemicals, Peptides, and Recombinant Proteins		
Tamoxifen	Millipore Sigma	T5648
Collagenase D	Millipore Sigma	11088882001

(Continued on next page)

Continued

REAGENT or RESOURCE	SOURCE	IDENTIFIER
Dispase II	Millipore Sigma	04942078001
Collagenase from Clostridium histolyticum	Millipore Sigma	C6885
Hoescht 33342	Millipore Sigma	B2261
Propidium iodide	Thermo Fisher	P1304MP
5-ethynyl-2'-deoxyuridine (EdU)	Thermo Fisher	E10415
DAPI	Thermo Fisher	D3571
VectaShield mounting medium with DAPI	Vector Laboratories	H-1200
DMEM	Thermo Fisher	11965-092
FBS	Thermo Fisher	1455501
FBS GemCell	Gemini Bio Products	100-500
Penicillin/Streptomycin	Thermo Fisher	151140-112
L-glutamine	Thermo Fisher	25030
FGF2	PeproTech	100-18B
Paraformaldehyde	PolySciences Inc	00380-1
2-methylbutane	Millipore Sigma	270342
AquaPolymount	PolySciences Inc	18606
Tissue Tek OCT compound	Sakura Finetek	4583
TGFB1	R&D	240-B
Goat serum	Gemini Bio Products	100-109
Donkey serum	Gemini Bio Products	100-151
Bovine serum Albumin	Millipore Sigma	A7030
Sodium borohydride	Millipore Sigma	213462
MesenCult Adipogenic Differentiation Kit (Mouse)	Stem Cell Technologies	05507
MesenCult MSC basal medium (Mouse)	Stem Cell Technologies	05505
Nilotinib	Novartis	N/A
Corn oil	Millipore Sigma	C8267
Magnesium chloride	Millipore Sigma	M1028
Glutaraldehyde	Millipore Sigma	G5882
Sodium chloride	Millipore Sigma	59222C
Nonidet P40 substitute	Millipore Sigma	74385
Deoxycholate	Millipore Sigma	D6750
Potassium ferricyanide	Millipore Sigma	P8131
Potassium ferrocyanide	Millipore Sigma	P3289
5-bromo-4-chloro-3-indolyl- β -D-galactopyranoside	Thermo Fisher	15520-018
Isoflurane	Piramal	NDC 66794-017-25
SuperScript II Reverse Transcriptase	Thermo Fisher	18064014
(-)-Isoproterenol hydrochloride	Millipore Sigma	I6504
Calcium Chloride	Millipore Sigma	C1016
Triton X-100	Millipore Sigma	T8787
Zamboni fixative	Newcomersupply	1459A
2,2,2 tribromoethanol	Millipore Sigma	T48402
tert amyl alcohol	Millipore Sigma	152463
Critical Commercial Assays		
RNeasy plus micro kit	QIAGEN	74034
Bioanalyzer 2100 RNA 6000 Nano kit	Agilent	5067-1511
Bioanalyzer 2100 RNA 6000 Pico kit	Agilent	5067-1513
TruSeq Stranded mRNA library kit	Illumina	RS-122-2103
Chromium Single Cell A Chip Kit, 48 rxns	10x Genomics	120236

(Continued on next page)

Continued

REAGENT or RESOURCE	SOURCE	IDENTIFIER
Chromium Single Cell 3' Library & Gel Bead Kit v2, 16rxns	10x Genomics	120237
Chromium i7 Multiplex Kit 96 rxns	10x Genomics	120262
NSQ 500/550 Hi Output KT v2.5 (150 CYS)	Illumina	20024907
NSQ 500 hi- Output KT v2 (150 CYS)	Illumina	FC-404-2002
NSQ 500/550 Hi Output KT v2.5 (75 CYS)	Illumina	20024906
NSQ 500 hi- Output KT v2 (75 CYS)	Illumina	FC-404-2005
Click-iT Plus EdU Pacific Blue Flow Cytometry Assay Kit	Thermo Fisher	C10418
Click-iT EdU Cell Proliferation Kit for Imaging, Alexa Fluor 647 dye	Thermo Fisher	C10340
Deposited Data		
Gene Expression Omnibus (GEO: GSE141929)	This paper	GEO: GSE141929
Experimental Models: Cell Lines		
C3H/10T1/2, Clone 8	ATCC	CCL-226
Experimental Models: Organisms/Strains		
B6.Cg- <i>Ndor</i> ^{1Tg(UBC-cre/ERT2)1Ejb} /2J	Jackson Laboratories	Jax stock number 008085
B6.Cg-Gt(ROSA)26Sortm14(CAG-tdTomato)Hze/J	Jackson Laboratories	Jax stock number 007914
B6.129S4-Pdgfratm11(EGFP)Sor/J	Jackson Laboratories	Jax stock number 007669
Hic1 ^{fl/fl}	Scott et al., 2019	N/A
Hic1 ^{CreERT2}	Scott et al., 2019	N/A
Hic1 ^{cit}	Pospichalova et al., 2011 ; PMID: 21309068	N/A
Pdgfra ^{CreERT2}	Chung et al., 2018 ; PMID: 29752282	N/A
<i>Col1a1</i> *3.6GFP	Kalajzic et al., 2002 ; PMID: 11771662	N/A
C57BL/6-CMV-b actin-EGFP	I. Weissman lab	N/A
DSG2 ^{mu} (DSG2 c.1672C > T, p.Q558X mutation)	A. Rampazzo lab	N/A
Software and Algorithms		
SDS 2.0 and SDS RQ Manager software	Thermo Fisher	N/A
NIS elements	Nikon	N/A
GraphPad Prism	GraphPad	N/A
Fiji	Schindelin et al., 2012 ; PMID: 22743772	https://imagej.net/Fiji/Downloads
Adobe Illustrator CS6	Adobe	N/A
FlowJo	BD	N/A
Basespace	Illumina	N/A
Bowtie 2	Langmead and Salzberg., 2012 ; PMID: 22388286	http://bowtie-bio.sourceforge.net/bowtie2/index.shtml
STAR	Dobin et al., 2013 ; PMID: 23104886	https://github.com/alexdobin/STAR
Cufflinks	Trapnell et al., 2010 ; PMID: 20436464	http://cole-trapnell-lab.github.io/cufflinks/
VisRseq	Younesy et al., 2015 ; PMID: 26328469	https://visrsoftware.github.io/
Microsoft Excel	Microsoft	N/A
Cellranger 2.0.1	10x Genomics	https://support.10xgenomics.com/single-cell-gene-expression/software/release-notes/2-0
R project for Statistical Computing	The R Project for Statistical Computing	https://www.rproject.org/

(Continued on next page)

Continued

REAGENT or RESOURCE	SOURCE	IDENTIFIER
RStudio Desktop	RStudio	https://rstudio.com/products/rstudio/
Seurat for R v2.2 and v.3	Satija R lab; Satija et al., 2015; PMID: 25867923. Stuart et al., 2019; PMID: 31178118	https://github.com/satijalab/seurat
Monocle 2 for R	Bioconductor	http://cole-trapnell-lab.github.io/monocle-release/docs/
Loupe Cell Browser	10x Genomics	https://support.10xgenomics.com/single-cell-gene-expression/software/visualization/latest/what-is-loupe-cell-browser
DAVID Bioinformatics Resources v.6.8	Huang et al., 2009b; PMID: 19131956	https://david.ncifcrf.gov/home.jsp
FACSDiva	BD Biosciences	N/A

LEAD CONTACT AND MATERIALS AVAILABILITY

Further information and requests for resources and reagents should be directed to and will be fulfilled by Dr. Fabio Rossi (fabio@brc.ubc.ca). This study did not generate new unique reagents.

EXPERIMENTAL MODEL AND SUBJECT DETAILS**Mice**

For generation of *Pdgfra*^{CreERT2} “knock-in” allele, a *CreERT2* polyA cassette and a FRT-flanked neo cassette were recombined into the start codon of *Pdgfra*. The construct was electroporated into TL1 (129S6/SvEvTac) ES cells. Properly targeted ES cells were identified through a combination of PCR and Southern analysis and these were injected into C57BL/6 blastocysts. Then the neo cassette was removed. *Pdgfra*^{CreERT2} mice are maintained on a C57BL/6 background (Chung et al., 2018).

Other mouse lines used include: B6.Cg-Gt(ROSA)26Sor^{tm14(CAG-tdTomato)Hze/J} (Jax stock number 007914; herein referred to as Rosa^{LSL-tdTomato}), B6.Cg-Ndor^{1Tg(UBC-cre/ERT2)1Ejb/2J}

(Jax stock number 008085; herein referred to as *Ubc*-CT2), B6.129S4-*Pdgfra*^{tm11(EGFP)Sor/J} (Jax stock number 007669); herein referred to as *Pdgfra* H2BGFP. All mice were maintained in (or as noted backcrossed to) a C57BL/6 background. *Col1a1**3.6GFP mice were a gift from Dr. David W. Rowe (Center for Regenerative Medicine and Skeletal Development, University of Connecticut Health Center; [Kalajzic et al., 2002]). C57BL/6-CMV-b actin-EGFP (GFP mice) were a kind gift from Dr. I. Weissman (Stanford University). Mice harboring *Hic1*-CT2, or *Hic1*^{Fil/LacZ} alleles were generated in the Underhill lab (Scott et al., 2019), while mice harboring *Hic1*-citrine reporter were generated by the Korinek lab (Pospichalova et al., 2011). For lineage tracing experiments, *Hic1*-CT2 mice were interbred with Rosa^{LSL-tdTomato} mice (Ai14 line, JAX stock 007914). For experiments involving conditional deletion of *Hic1*, *Hic1*^{Fil/Fil} mice were interbred with *Ubc*-CT2 or *Pdgfra*-CT2 mice. Transgenic mice with cardiac-specific overexpression of FLAG-tagged mutant human DSG2 (c.1672C > T, p.Q558X; DSG2^{mu}) were generated in the Rampazzo lab. Full-length mutant human DSG2 cDNAs were expressed under the control of mouse alpha-myosin heavy chain promoter. The transgenic mice were maintained on a C57BL/6 background. DSG2^{mu} mice were interbred with *Hic1*-CT2 or *Pdgfra*-CT2 mice. Allelic recombination under the *Pdgfra*-CT2, *Hic1*-CT2 or *Ubc*-CT2 alleles was induced by daily injections of 0.1 mg/g TAM in 100uL of corn oil for 5 consecutive days, administered intraperitoneally to animals > 8 weeks old. To control for TAM toxicity, all mice, including controls, were administered TAM and cardiac function was always performed at least 2 weeks after TAM to allow for a washout period.

Mice were housed under standard conditions (12 hr light/dark cycle) and provided food and water *ad libitum*. For all experiments, litter mates of the same sex were randomly assigned to experimental groups. Animals were maintained and experimental protocols were conducted in accordance with approved and ethical treatment standards of the Animal Care Committee at the University of British Columbia.

FAP primary culture

Cells were sorted from dissociated hearts using indicated gating strategies into high glucose (4.5g/L) Dulbecco's modified eagle medium (DMEM, Thermo Fisher), supplemented with 10% (v/v) fetal bovine serum (FBS; or 20% in clonal expansion studies), 10 ng/ml bFGF (PeproTech), 1% (v/v) Penicillin/Streptomycin (Thermo Fisher) and 2 mM L-glutamine (Thermo Fisher). Media was changed every 2-3 days. For adipogenic differentiation of bulk cultures from *Pdgfra* CT2 tdTomato mice, following 14 days of growth, medium was changed to MesenCult MSC basal medium (Stem Cell Technologies) supplemented with MesenCult adipogenic stimulatory supplement for mouse (Stem Cell Technologies) and 2 mM L-glutamine. Cells were cultured for an additional 14 days and adipogenesis

was assessed via immunostaining for the adipocyte marker perilipin using a rabbit anti-mouse perilipin A/B antibody (Sigma-Millipore). Images were collected using an Axiovert S100 (Zeiss) inverted microscope.

For *in vitro* differentiation studies, hearts from *Col1a1*-3.6GFP mice were digested and *Col1a1*-3.6GFP negative cells were grown for 3 days in high (4.5g/L) glucose DMEM (Thermo Fisher), supplemented with 10% v/v fetal bovine serum (FBS), 10 ng/ml bFGF (Peprotech), 1% (v/v) Penicillin/Streptomycin (Thermo Fisher) and 2 mM L-glutamine (Thermo Fisher) and treated with TGFβ1 (R&D; 1ng/ml), and/or Nilotinib (1uM) for one week before being analyzed.

For clonal expansion and developmental potential experiments, FACS sorted single *Pdgfra*-CT2 tdTomato⁺/SCA-1⁺ and SCA-1⁻, PDGFRα⁺/SCA-1⁺ and SCA-1⁻, and MCAM⁺/*Hic1*-CT2 tdTomato⁺ (MCAM⁺/*Hic1* CT2 tdtomato⁺ cells were sorted 2 days after TAM induction) cells were individually seeded in 96 well plates on a feeder layer of gamma irradiated mouse-derived C3H/10T1/2 cells. The cells were cultured in high glucose (4.5g/L) DMEM (Thermo Fisher), supplemented with 20% v/v FBS (GemCell™, Gemini BioProducts), 10 ng/ml bFGF (Peprotech), 2 mM L-glutamine (Thermo Fisher) and 1% (v/v) Penicillin/Streptomycin (Thermo Fisher) for 14 days. Colonies, defined as > 32 cells per well (5 or more cell divisions), were counted from images acquired by Incucyte S3 system (Essen Bioscience) and, following fixation with 2% paraformaldehyde, were immunostained for the adipocyte marker perilipin using a rabbit anti-mouse perilipin A/B antibody (Sigma-Millipore). Images were collected using an Axio Vert S100 (Zeiss) inverted microscope.

METHOD DETAILS

Induction of cardiac damage and Nilotinib treatment

Cardiac damage was induced by subcutaneous injection of 100 mg/kg of isoproterenol (Millipore-Sigma) for five consecutive days. To experimentally induce myocardial infarctions, animals were placed on a heated pad and ventilated using a mixture of oxygen and isoflurane until surgical anesthesia. Hair was clipped on the area of incision corneal lubricant was applied. Skin was surgically scrubbed with alcohol and Bupivacaine was administered SQ at the incision site. An incision through the skin and then rib cage was made, and then a retractor was used to visualize the heart. Using an 8-0 polypropylene suture, a branch of the left anterior descending (LAD) artery was ligated. Wound was then closed using a 6-0 vicryl suture in a horizontal mattress pattern (Kolk et al., 2009). *In vivo* pre or post LAD Nilotinib (Novartis) treatment was achieved by daily intraperitoneal injections of 25 mg/kg at the indicated times.

Heart digestion and fluorescence-activated cell sorting (FACS)

FAPs were released from the cardiac ventricles using a previously described protocol with modifications (Joe et al., 2010). Mice were sacrificed, their hearts carefully excised and cut into 2mm pieces. A single cell suspension was made by digesting tissue for 30 minutes at 37°C in Collagenase type II solution (Millipore Sigma; 500uL per heart of 2.5 U/mL) in 10 mM CaCl₂. Suspensions were then centrifuged at 800 rpm and supernatant decanted. This was repeated twice followed by incubation for 1 hour at 37°C in a 500uL solution containing Collagenase D (Millipore Sigma 11 088 882 001; 1.5 U/ml), Dispase II (Millipore Sigma 04 942 078 001; 2.4 U/ml) and 10 mM CaCl₂. Digested material was triturated by pipetting and, following washing and filtration through 40 μm cell strainer filters, cell preparations were washed, centrifuged at 1500 rpm for minutes and incubated with primary antibodies against cell markers for 30 min at 4°C in supplemented PBS containing 2 mM EDTA and 2% FBS (FACS buffer) at ~3 × 10⁷ cells/mL. To enrich for FAPs from this whole heart mononuclear suspension, cells were selected for the expression of various cell surface markers including CD45, CD31 and SCA-1. The Lin negative fraction was considered to be negative for CD45 and CD31. This was accomplished by incubation with a cocktail containing anti-CD45-APC or anti-CD45-FITC (ebioscience, clone 30-F11, 1:500 and 1:1000, respectively) and anti-CD31-APC or anti-CD31-FITC (BD Biosciences, clone MEC13.3, 1:300 for both fluorophores). The Lin negative population was further sub-fractionated based on SCA-1 expression by the addition of anti-Ly-6A/E (Sca-1)-PE-Cy7 (eBioscience clone D7, 1:3000) to the above antibody cocktail. After incubation, 15 mL of FACS buffer was added to dilute the antibodies prior to centrifugation at 1500 rpm for 5 mins. The pellet was resuspended in FACS buffer containing Hoechst 33342 (Sigma B2261) to a final concentration of 4 μM and propidium iodide (PI; Thermo Fisher) to a final concentration of 1 μg/mL. Stained cells were sorted using a BD Influx, and Hoechst, PI and forward/side scatter parameters were used to identify viable single cells for all FACS enrichments. Sorted cells were collected into sort media made of DMEM, 20% FBS (Thermo Fisher), L-glutamine (2 mM), 1% (v/v) Penicillin/Streptomycin (Thermo Fisher) in cooled siliconized microcentrifuge tubes (Thermo Fisher; 02-681-320).

Analysis of FAP proliferation

For *in vivo* proliferation assays, EdU (Thermo Fisher) was dissolved in PBS at 2 mg/ml solution and it was administered daily by intraperitoneal injection (40 mg/kg). For flow cytometric analysis, cells were first stained for surface markers, then stained for EdU incorporation using the Click-iT Plus EdU Pacific Blue Flow Cytometry Assay Kit (Thermo Fisher C10418) as described in the manufacturer's manual. Analysis was performed on LSRII (Becton Dickinson) equipped with three lasers. Data were collected using FACSDiva software (BD Biosciences). Cell sorting was performed on a FACS Influx (Becton Dickinson) or FACS Aria (Becton Dickinson) sorters. Sorting gates were strictly defined based on fluorescence minus one stains. Flow cytometry data analysis was performed using FlowJo 10.4.1 software (BD Biosciences). For fluorescence imaging of EdU, *Pdgfra* H2BGFP mice heart sections (10 μm) were stained with the collagen I and EdU incorporation using the Click-iT EdU Cell Proliferation Kit for Imaging, Alexa Fluor 647 dye (Thermo Fisher C10340) as described by the manufacturer.

***in situ* X-gal staining and immunofluorescence/histology**

For *in situ* X-gal staining, mice were terminally anesthetized by intraperitoneal injection of Avertin (400 mg/kg), the chest was opened and hearts were perfused with cold LacZ fixative (100 mM MgCl₂, 0.2 % glutaraldehyde, 5 mM EDTA in PBS), then dissected and immersed in LacZ fixative for 3 hours on ice.

For detection of native tdTomato expression, mice heart samples were collected following transcardiac perfusion. For this purpose, mice received an intraperitoneal injection of Avertin (400 mg/kg), and then were perfused transcardially with 10 mL PBS/2 mM EDTA, followed by 10 mL of 4% paraformaldehyde (PFA). The excised hearts were fixed in 4% PFA for 24 hours at 4°C. When immunostaining for collagen I, hearts were fixed with Zamboni fixative (2% paraformaldehyde, 0.2% picric acid in phosphate-buffered saline (PBS), pH 7.6; Newcomersupply) for 2 hours at room temperature.

For cryosectioning, samples were washed 3 times for 30 mins with PBS then incubated in a cryoprotective sucrose solution (30%) overnight before embedding into OCT compound (Tissue Tek 4583) in disposable plastic cryomolds (Polysciences 18646A) and frozen in an isopentane bath cooled by liquid nitrogen. Cryosections were cut with a Leica CM3050S cryostat at a thickness of 10–20 µm and mounted onto Superfrost Plus slides (VWR 48311-703).

For detection of collagen fibers in the heart, sections were stained using Masson's Trichrome Stain as previously described (Bo-stick et al., 2012). For detection of LacZ on sections, *in situ* LacZ staining with X-gal was carried out, where slides were incubated overnight at 37°C in a humidified chamber with the LacZ staining solution (2 mM MgCl₂, 0.01 % Deoxycholate, 0.02% NP40, 5 mM potassium ferricyanide, 5 mM potassium ferrocyanide and 1mg/mL 5-bromo-4-chloro-3-indolyl-β-D-galactopyranoside). Slides were counter-stained with nuclear fast red and mounted with Aqua Polymount. For additional IF staining of LacZ stained samples, freshly stained slides were subsequently washed with PBS for 3 X 5 mins and IF staining was carried out as described below.

For Immunofluorescence staining, slides were thawed at room temperature, washed 3 × 10 mins in PBS and incubated for 1 h in PBS containing 10 mg/mL sodium borohydride (Sigma 213462) to quench autofluorescence. Then, slides were washed with PBS and incubated in block solution containing 10% normal goat serum (NGS; or normal donkey serum if antibody is raised in goat), 0.2% Triton X-100 and 5% bovine serum albumin (BSA; Sigma A7030) for 60 mins at room temperature prior to incubation with primary antibodies (listed in the Key resources table below) overnight at 4°C. Secondary antibodies conjugated to Alexa Fluor 488, 555 or 647 (Molecular Probes, Thermo Fisher) were typically diluted 1:200 and applied to the slides for 90 mins at room temperature. After each antibody incubation, 3 × 5 min PBS washes were performed, and sections were counterstained with DAPI (600 nM) and mounted with Aqua Polymount (Polysciences 18606) or mounted with Vectashield mounting medium with DAPI (Vector Laboratories).

Image acquisition and quantification

Widefield epifluorescence and bright field microscopy images were collected on a Nikon Ni-E upright or a Zeiss Axio Vert S100 microscope. Confocal images in Figures 5C, 5D, 5F, 5G, 6B, 6C, 7B, S1C, S6C, and S6D were collected using a Nikon Eclipse Ti inverted microscope equipped with a C2Si confocal system, confocal images in Figure 2A were collected using a Leica SP5X White Light Laser Confocal Microscope equipped with a Koheras white light laser source whose emission covers the 470–670nm spectrum of wavelengths and confocal images in Figures S1H, S1I, S2A, S2D, and S3B were collected using a Leica SP8 DLS confocal microscope with a tunable prism-based spectral detector and a GaAsP hybrid detector. Image processing was performed using NIS Elements for images taken with the Nikon microscopes or LAS X for images taken with the Leica microscopes. Figures were assembled using Adobe Illustrator CS6 (Adobe). Colocalization of tdTomato with collagen I immunostaining in heart sections in Figure 5 was determined using ImageJ (Fiji v.1). Split channel images were generated, and the area of fibrosis was highlighted. Colocalization was determined using the colocalization thresholds plugin and a colocalized pixel map image was generated with constant intensity for colocalized pixels. % colocalization was determined as the % channel volume (number of voxels which have both channel 1 (Collagen I) and channel 2 (tdTomato) intensities above threshold determined using Pearson's coefficient expressed as a percentage of the total number of voxels for collagen I channel above its threshold.

Echocardiography

Cardiac function and dimensions were evaluated by two-dimensional transthoracic echocardiography. Echocardiographic image acquisition was carried out using the Vevo2100 system (Fujifilm Visualsonics). Mice were anaesthetized with 3%–4% isoflurane (Piramal) in 100% oxygen. Following induction, mice were placed on a heated handling table and all limbs were connected to the electrodes on the table using electrode cream, then hair was removed from the thoracic region using a depilatory applied for 1 minute. Lubricant ointment was applied to the eye and anesthesia and body temperature were maintained at 1%–1.5% isoflurane and 37 ± 0.5°C, respectively. A rectal thermometer was used to monitor body temperature more accurately. M-mode 2-dimensional echocardiography in the long axis view was used to measure contractile function and cardiac dimensions in Figure 4, while short axis view was used in Figures 6 and 7. The 4-chamber apical view was used to measure E/A ratio and other diastolic function parameters. All measurements were performed by an experienced operator blinded to the mouse genotypes.

Treadmill forced exercise test

Hic1 cKO mice and their controls were subjected to low intensity short periods of exercise for 5 consecutive days for training purpose on a rodent treadmill equipped with shock grids to deliver very low level electrical stimulus when mice stop running (Columbus Instruments). After 2 days of rest, mice were run on the treadmill at a constant velocity of 10 m/min and the distance traveled before fatigue (the time point at which mice are electrically shocked 3 consecutive times and do not respond by continuing to run) was determined. Alternatively, mice were subjected to increasing treadmill velocities (1 m/min incremental increase every 50-m run) and the velocity at which mice displayed fatigue was determined.

Quantitative Reverse Transcription PCR

To investigate the expression of genes related to extracellular matrix deposition, RNA isolation was performed using RNeasy mini kits (QIAGEN) and 250 ng of RNA were converted to cDNA using reverse transcription performed using the Superscript II Reverse Transcriptase (Thermo Fisher). Fibrogenic gene expression analysis was performed using Taqman Gene Expression Assays for *Tgfb1*, *Vim*, *Ctgf*, *Col1a1*, *Fn1* (Thermo Fisher) on a 7900HT Real Time PCR System (Thermo Fisher). Data were acquired and analyzed using SDS 2.0 and SDS RQ Manager software (Thermo Fisher).

Gene expression profiling – popRNA-seq

Total RNA was isolated using RNeasy plus micro kits (QIAGEN, 74004) as per manufacturer's instructions. Sample integrity was tested on an Agilent Bioanalyzer 2100 RNA 6000 Nano or Pico kits (Agilent, 5067-1511 and 5067-1513, respectively). RNA samples with an RNA Integrity Number > 8 were used to prepare libraries following the standard protocol for the TruSeq Stranded mRNA library kit (Illumina) on the Illumina Neoprep automated microfluidic library prep instrument. Paired end sequencing was performed on the Illumina NextSeq 500 using the High Output 150 cycle Kits (Illumina).

RNA-seq Bioinformatic Analyses

Illumina sequencing output generated bcl files were de-multiplexed by bcl2fastq2. Demultiplexed read sequences were then aligned to the Mouse Genome mm10 reference sequence using TopHat splice junction mapper with Bowtie 2 (<http://ccb.jhu.edu/software/tophat/index.shtml>) or STAR (<https://www.ncbi.nlm.nih.gov/pubmed/23104886>) aligners. Assembly and differential expression was estimated using Cufflinks (<http://cole-trapnell-lab.github.io/cufflinks/>). The heatmap in Figure 3C was generated using VisRseq (Younesy et al., 2015). The heatmap was generated from the Z-score of the different genes at the specified time points.

Single Cell RNA-seq

Single cell suspensions were prepared by digesting the hearts and FACS-sorting target population into sterile-filtered culture medium (DMEM containing 5% FBS). Second sorting in 35 μ L medium was done to ensure high purity and quality of the cells. In the *Pdgfra* H2BGFP and *Hic1* citrine datasets, cells from different mice were pooled after incubation with hashing antibodies against MHC I and CD45 (TotalSeq® A0301-A0304, Biolegend). In the *Pdgfra* H2BGFP dataset, 2 undamaged hearts and 2 7-day LAD-ligated hearts were pooled and in the *Hic1* citrine dataset, 3 hearts were pooled after hashing. After the target cell suspension was examined for quality and cells counted using a hemocytometer, they were delivered into a Chromium Controller (10x Genomics), captured and libraryed with the Chromium single cell 3' reagent kit v2 (10x Genomics). cDNA libraries were sequenced on a Nextseq 500 (Illumina) to a minimum depth of 20,000 mean reads per cell. Demultiplexing and alignment to the modified mm10 reference genome was performed using the cellranger count pipeline (10x Genomics). Filtering of low quality cells (cells with $\geq 10\%$ mitochondrial genes and/or < 200 genes), principal component analysis (PCA), clustering, non-linear dimensionality reduction, differential expression, graphical output, merging and subsetting of datasets was performed using Seurat R package (Satija Lab, v.2.2; (Satija et al., 2015)). Subsetting was performed by excluding the clusters that expressed pericytic markers in order to focus only on the cFAPs when building a phylogenetic tree or merging the datasets. Subsequently, PCA, graph-based clustering, t-SNE or UMAP and Wilcoxon rank sum test for differential expression were performed with Seurat R package. Gene ontology analysis for the 50 most differentially upregulated genes in the different clusters was performed using the DAVID Bioinformatics Resources (Huang et al., 2009a, 2009b) (v.6.8). Single Cell trajectory analysis was performed using Monocle (Trapnell lab, v.2.1) (Trapnell et al., 2014). Cells were clustered and then dimensionality reduction was performed, followed by ordering cells along the trajectory based on the 200 most differentially expressed genes using reverse-graph embedding (DDRTree). Then cells were ordered in pseudotime and expression kinetics of selected genes was plotted in branched pseudotime. Datasets in Figure 1E were merged using the Seurat multi-dataset anchoring algorithm (Satija lab, v.3; [Stuart et al., 2019]).

QUANTIFICATION AND STATISTICAL ANALYSIS

All data is represented as mean \pm standard error of the mean (SEM) and the sample number is indicated in the figure legends, where n indicates the number of animals used per group. Data in all figures were obtained from at least 2 independent experiments involving different mice. Sample size determination was based on anticipated variability and effect size that was observed in the investigator's

lab for similar experiments. Statistical analysis was performed using unpaired Student's t test for analysis between 2 groups. For comparison between 3 or more groups, one- or two-way ANOVA was performed (with repeated-measures in case of a time course). Bonferroni or Holm-Sidak (in case of preselected comparisons) post hoc test was performed to correct for multiple comparisons using Graphpad Prism® version 7 (GraphPad Software, La Jolla California USA). Sample size and/or replicate number for each experiment is indicated in the figure legends. Results with p values of less than 0.05 were considered statistically significant.

DATA AND CODE AVAILABILITY

The bulk and single cell RNA sequencing datasets generated during the current study are available in the NCBI Gene Expression Omnibus. The accession number for the data reported in this paper is GEO: GSE141929. Software used to analyze the data is either freely or commercially available.